The Impact of Nanoparticle Shape on the Bioconvection Flow Containing Magnetotactic Bacteria

Merve Gurbuz-Caldag[a,*]

a. Department of Mathematics, TED University, Ankara, Türkiye

* Corresponding author: merve.gurbuz@tedu.edu.tr (Merve Gurbuz-Caldag)

Keywords

Nanoparticle shape;
Bioconvection;
RBF;
Magnetotactic bacteria;
Curve fitting.

Abstract

This study investigates the influence of nanoparticle shape on the bioconvection flow of a magnetite-water nanofluid containing magnetotactic bacteria in a curved cavity. The main aim is to examine how different nanoparticle shapes, which are spherical, brick, cylinder, platelet and blade, affect the heat and mass transfer characteristics alongside the swimming behavior of bacteria. The novelty of this research lies in the first-time analysis of nanoparticle shape impacts on bioconvection in a complex curved geometry, combined with the application of the radial basis function method to solve the nondimensional governing equations. Curve fitting is also employed to model the average Nusselt and Sherwood numbers as functions of nanoparticle shape and physical parameters. The results indicate that as Rayleigh number increases, spherical particles yield the highest increase in heat transfer rate by 313.6%, while platelet-shaped particles reduce the mass transfer rate by 31.60%. Peclet numbers enhances the average density of bacteria for spherical nanoparticles by 14245%. As the amplitude of the wavy wall rises, the improvement in all average transport rates becomes more pronounced for platelet-shaped nanoparticles compared to other. By providing a high-accuracy predictive framework with a small mean squared error, this study establishes a practicle roadmap for engineers to select optimal particle shapes for bio-microfluidic design.

Highlights

- The impact of nanoparticle shape on heat and mass transfer of magnetite-water nanofluid flow is analyzed in a curved cavity filled by magnetotactic bacteria for the first time.
- RBF method is implemented to solve the governing equations for different values of physical parameters.
- Curve fitting method is firstly employed for modeling the average Nusselt and Sherwood numbers.
- Fitting functions of the average Nusselt and Sherwood numbers are obtained in terms of nanoparticle shape and each physical parameter.

Graphical Abstract

Graphical abstract is shown in Fig. 1.

1. Introduction

Nanofluids composed of the base fluid and nanoparticles are used in the heat and mass transfer problems due to the variety of applications such as cooling electronic devices, microelectronic devices, drug delivery systems, solar panels, etc. Choi [1] first conducted the theoretical study on the improvement of thermal conductivity (tc) of fluid including copper nanoparticles. Gumgum and Tezer-Sezgin [2] implemented the dual reciprocity boundary element method (DRBEM) to the natural convection flow of nanofluid for the variation of Rayleigh number (Ra), volume fraction (vf). It is reported that the augmentation of vf enhances the heat transfer. Jalili et al. [3] conducted an experimental investigation on the performance of refrigeration cycles using carbon nanotube (CNT) nanoparticles. Their results revealed that increasing the concentration of CNT particles significantly enhances the temperature gradient between the evaporator entry and discharge compared to pure water. In [4], Lattice Boltzmann method is applied to investigate nanofluid hydrothermal treatment in a cubic cavity in the presence of magnetic field. The influences of distinct nanoparticles and aspect ratio (ar) of the enclosure are investigated on the natural convection in [5]. It is observed that the heat transfer enhances as ar decreases. Sheikholeslami [6,7] anlayzed the Lorentz force impact on nanofluid in different regions of porous enclosures. Sayyou et al. [8] examined the convective flow of Cu-water in an inclined cavity with gravitational modulation. It is presented that the amplitude of gravity develops the heat transfer. In [9], the mixed convection of Al2O3-Cu/water hybrid nanofluid is conducted over a permeable vertical plate influenced by magnetic and radiation parameters. Their findings emphasize that optimizing nanoparticle concentration volume is crucial for maintaining flow stability and maximizing thermal performance in magnetohydrodynamic systems. Li et al. [10] explored the transient thermal behavior and entropy generation of a similar hybrid nanofluid within a square finned cavity containing a cylindrical obstruction. It is reported that increasing the Richardson number at various Reynolds numbers expands the temperature distribution and enhances both horizontal and vertical velocities. Hajizadeh et al. [11] explored the potential of hybrid nanofluids within a non-Newtonian Maxwellian model, focusing on thermal management in specialized curved channels. It is demonstrated that the integration of both single and multi-layered CNTs into engine oil-based nanofluids offers substantial potential for improving thermal exchange performance. A comprehensive review conducted by Khalatbari et al. [12] assesses the recent advancements

in hybrid nanofluids, providing unique insights into their thermophysical properties through both experimental measurements and diverse numerical approaches such as FEM and Akbari–Ganji method (AGM). In [13], Python programming is used to explore the influence of magnetic field strength on a two-dimensional squeezing nanofluid flow confined between two parallel plates. It is shown that as the Prandtl number increases, the temperature and thermal properties of the nanofluid flow increase.
Magnetite Fe_3O_4 nanoparticles are used in the applications of science, technology and medicine which are drug delivery, magnetic resonance imaging (MRI), extraction of heavy metals, biosensors [14,15]. Sheikholeslami [16] investigated the impact of magnetic source on Fe_3O_4-water nanofluid by using CVFEM. It is shown that Lorentz force enhances the thickness of thermal boundary layer. In [17], finite volume method (FVM) is implemented to free convection flow in baffle C shaped cavity filled by magnetite-water in the presence of magnetic field. They reported that the rise in the baffle length increases the heat transfer. Battira et al. [18] applied FVM to examine the heat transfer of magnetite-water nanofluid in the variation of Ra, vf and Hartmann number (Ha). It is shown that the direction of magnetic field impacts the heat transfer. Jalili et al. [19] investigated two-dimensional ferrofluid flow within semi-porous channels under the influence of Lorentz forces. Their comparative analysis using AGM and FEM demonstrated that increasing the Hartmann number suppresses velocity profiles, while the vf of nanoparticles showed a minor impact on shear stress. In [20], the MWCNT-Fe_3O_4-water hybrid nanofluid is considered in a wavy micro-channel under the impact of the magnetic field. The wavy of the channel is classified as uniform, increasing and decreasing amplitudes. It is noted that increasing amplitude channel improves the heat transfer.
Nanoparticle shape has an important impact on the heat transfer. Timofeeva et al. [21] analyzed the influence of nanoparticle shape on the thermal conductivity and viscosity of alumina-EG/water nanofluid. They reported that viscosity depends on the shape and surface properties of nanoparticles. Selimefendigil et al. [22] reported that $\overline{Nu}$ attains maximum value for cylindrical shape of SiO_2-water nanofluid in a cavity with flexible wall containing cylinder. In [23,24], the impact of different nanoparticle shapes of Fe_3O_4-H_2O and CuO-H_2O in the permeable cavity subjected to magnetic source and uniform magnetic field are analyzed, respectively. The highest heat transfer is obtained for platelet shape of nanoparticle in both studies. Sheikholeslami et al. [25] found the same impact of platelet on the heat transfer in the porous curved cavity filled by Fe_3O_4-water. The entropy generation of MHD flow over a stretching sheet is investigated for different nanoparticle shapes of Al_2O_3-water nanofluid in [26]. The entropy production on the cold side is more for Os shape. Kim et al. [27] studied the impacts of vf and the shape of the nanoparticle on the different types of nanofluids subjected to the magnetic field. They reported that the lamina shaped nanoparticle enhances the heat transfer more than the other nanoparticle shapes.
The integration of machine learning techniques has emerged as a powerful tool for analyzing nanofluid systems. In [28], both the artificial neural network (ANN) and surface method are implemented to predict the viscosity of MgO-water nanofluid in terms of vf of nanoparticles, temperatures, and shear rates. Fitting surfaces for different vfs are presented and the absolute error of fitting method is obtained 0.0206. He et al. [29] obtained the model of k_{nf} of ZnO-Ag nanofluids by using ANN. They showed that surface fitted on the experimental data and calculated absolute error. The surface fitting function of k_{nf} of EG/MWCNT-Al2O3-water hybrid nanofluid is obtained in terms of vf and temperature of the nanofluid by Fuxi et al. [30]. Rostami et al. [31] predicted k_{nf} of MWCNT-CuO/water hybrid nanofluids with the use of ANN and fitting methods. In [32], ANN is employed to predict the viscosity and tc of Fe_3O_4-water. In this process, the experimental dataset is obtained for the variation of temperature and vf. Chari et al. [33] investigated the combined effects of MHD convection, Joule heating, and radiation on hybrid nanofluid flow within a porous medium between rotating disks. By employing AGM to solve the transformed nonlinear governing equations, they provided a detailed sensitivity analysis through ANOVA. Their findings highlighted that the temperature profile is enhanced by magnetic field strength, while the Sherwood number shows a positive correlation with the chemical reaction parameter.
The bioconvection is generated by the movement of microorganisms through light, gravity, oxygen and magnetic field. Many researchers have been studied the bioconvection problems in different geometries including oxytactic [34–37], gyrotactic [38–42] and magnetotactic bacteria [43–45]. In addition to traditional numerical solutions, machine learning algorithms have recently been employed as a robust computational tool for analyzing bioconvectional problems. Chandra and Das [46] conducted a study on ANN model for the estimation of nanofluid flow over a stretchable vertically inclined surface containing gyrotactic bacteria. In [47], the average Nusselt, Sherwood and motile microorganism numbers of the mixed bioconvection flow of nanofluid of oxytactic bacteria through a porous cavity under the effect of periodic magnetic field is modeled using Light Gradient Boosting Machine algorithm. Mahboobtosi et al. [48] conducted a comprehensive study on the behavior of nanofluids containing microorganisms over a three-dimensional moving surface. By incorporating bioconvection and anisotropic slip effects, they developed a predictive ANN model trained on numerical data. Kiratli et al. [49] utilized the radial basis function (RBF) collocation method to generate a comprehensive dataset for the NN modeling of Cu-water nanofluid flow involving oxytactic bacteria. By numerically solving the governing equations under the influence of a magnetic source, they developed a predictive model that achieves high accuracy with even a single hidden layer. This approach demonstrates that RBF-generated datasets can effectively train NN to provide physical outputs such as average Nusselt and Sherwood numbers.
The aforementioned studies focused on the impact of different nanoparticle materials, volume fraction, cavity geometries, magnetic field and bacteria on the heat transfer. Also, nanoparticle shape effect on the heat transfer of nanofluid flow is analyzed. However, the interaction between biocovection flow generated by bacteria and nanoparticle shape has not been considered yet. To address this research gap, the present study investigates how nanoparticle shape influences the heat and mass transfer of bioconvection flow in a curved cavity filled by Fe_3O_4-water in the presence of magnetotactic bacteria. Radial basis function approximation (RBF) method is implemented to find the numerical results of this bioconvection problem for different problem parameters which are Rayleigh (Ra), bioconvection Rayleigh (R_b), Peclet (Pe) and Lewis (Le) numbers, nanoparticle shape parameter (n_{sh}) and the amplitude of the wall (a). After generating numerical data, surface fitting functions of the average

Nusselt, Sherwood numbers are obtained in terms of n_{sh} versus each parameter. Also, surfaces including the average number of bacteria and the minimum value of stream function are fitted on the numerical data. In each case, mean square error (mse) is calculated to ensure the accuracy of the model.

2. Physics of the Problem

The two-dimensional, steady natural convection flow of Fe_3O_4-water nanofluid including magnetotactic bacteria (MB) is considered in a square cavity with curved top and bottom walls which is shown in Fig. 2. Natural convection arises from the left hot wall from the right cold wall. The adiabatic top and bottom walls are constructed by

$$\begin{aligned} y_t(x) &= 1 + a\sin(\pi x), x \in [0,1] \\ y_b(x) &= -a\sin(\pi x), x \in [0,1], \end{aligned} \tag{1}$$

where a is the amplitude of the wall. Bioconvection is obtained from the movement of the MB.
Buoyancy effect is included by Boussinesq approximation due to the temperature difference and density, while the Joule heating, the radiation, Thermophoresis and Brownian motion effects, and the viscous dissipation are neglected.

A single phase model for Fe_3O_4-water nanofluid is used and the physical properties are stated as [50]

$$\rho_{nf} = (1-\phi)\rho_f + \phi\rho_s, \tag{2}$$

$$(\rho c_p)_{nf} = (1-\phi)(\rho c_p)_f + \phi(\rho c_p)_s, \tag{3}$$

$$(\rho\beta)_{nf} = (1-\phi)(\rho\beta)_f + \phi(\rho\beta)_s, \tag{4}$$

$$\alpha_{nf} = \frac{k_{nf}}{(\rho c_p)_{nf}}, \tag{5}$$

$$\frac{k_{nf}}{k_f} = \frac{k_s + (n_{sh}-1)k_f + (n_{sh}-1)\phi(k_s - k_f)}{k_s + (n_{sh}-1)k_f + (n_{sh}-1)\phi(k_f - k_s)}, \tag{6}$$

where subindices *nf, f, s* denote the nanofluid, fluid and solid, respectively, ρ is the density, β is the thermal expansion coefficient, c_p is the specific heat, α is the thermal diffusivity, ϕ is the solid vf and k_{nf} is the nanofluid tc which is given in [51]. n_{sh} is empirical shape factor of nanoparticle. The dynamic viscosity of nanofluid μ_{nf}, which is modeled by [21,52], is provided as

$$\mu_{nf} = \begin{cases} \mu_f(1-\phi)^{-2.5} & \text{if } n_{sh} = 3 \text{ (Spherical)} \\ \mu_f(1 + C_1\phi + C_2\phi^2) & \text{otherwise} \end{cases} \tag{7}$$

where C_1 and C_2 are constants stated in Table 1. Thermophysical properties of water and Fe_3O_4 are tabulated in Table 2.

Based on the above information, this problem is modeled by the dimensional equations given in [43,53,54].

Continuity Equation:

$$\frac{\partial u'}{\partial x'} + \frac{\partial v'}{\partial y'} = 0 \tag{8}$$

Momentum Equations:

$$\begin{aligned} &\nu_{nf}\nabla^2 u' = u'\frac{\partial u'}{\partial x'} + v'\frac{\partial u'}{\partial y'} + \frac{1}{\rho_{nf}}\frac{\partial p'}{\partial x'} \\ &\nu_{nf}\nabla^2 v' = u'\frac{\partial v'}{\partial x'} + v'\frac{\partial v'}{\partial y'} + \frac{1}{\rho_{nf}}\frac{\partial p'}{\partial y'} + \frac{g}{\rho_{nf}}\left(\gamma\Delta\rho n' - (\rho\beta)_{nf}(T'-T_c)\right) + \frac{g}{\rho_{nf}}(\rho_s - \rho_f)\beta_s(C' - C_{\min}) \end{aligned} \tag{9}$$

Energy Equation:

$$\alpha_{nf}\nabla^2 T' = u'\frac{\partial T'}{\partial x'} + v'\frac{\partial T'}{\partial y'} \tag{10}$$

Nanoparticle Concentration Equation:

$$D_c\nabla^2 C' = u'\frac{\partial C'}{\partial x'} + v'\frac{\partial C'}{\partial y'} + \delta n' \tag{11}$$

The Number of Microorganism Equation:

$$\frac{\partial}{\partial x'}\left(u'n' + \frac{bW_c}{\Delta C'}\frac{\partial C'}{\partial x'}n' - D_n\frac{\partial n'}{\partial x'}\right) + \frac{\partial}{\partial y'}\left(v'n' + \frac{bW_c}{\Delta C'}\frac{\partial C'}{\partial y'}n' - D_n\frac{\partial n'}{\partial y'}\right) = 0 \tag{12}$$

In these equations, ν is the kinematic viscosity, u',v' are the velocity components, p' is the pressure, g is the gravitational acceleration, γ is the mean volume of microorganism, D_c is the diffusivity of nanoparticle concentration, n is the density/number of bacteria, W_c is the maximum cell swimming speed, b is the chemotaxis constant, D_n is the diffusivity of microorganism, T' is the temperature, C' is the concentration, $\delta n'$ is the Fe_3O_4 consumption by the bacteria, $\Delta C' = C_h - C_{\min}$ and $\Delta\rho = \rho_{cell} - \rho_{nf}$.

The non-dimensional transformation parameters are introduced as [55]

$$(x,y)=\frac{1}{L}(x',y'),\ (u,v)=\frac{L}{\alpha_f}(u',v'),\ p=\frac{L^2}{\rho_f\alpha_f^2}p',\ T=\frac{T'-T_c}{\Delta T},\ C=\frac{C'-C_{\min}}{\Delta C},\ N_m=\frac{n'}{n_0}, \tag{13}$$

where L is the characteristic length, ΔT is the temperature difference between hot and cold walls, ΔC is the concentration difference and n_0 is the reference average number of bacteria.

Using the non-dimensional parameters Eq. (13), non-dimensional Eqs. (8)-(12) are obtained by

$$\frac{\partial u}{\partial x}+\frac{\partial v}{\partial y}=0, \tag{14}$$

$$\frac{\nu_{nf}}{\nu_f}Pr\nabla^2 u = u\frac{\partial u}{\partial x}+v\frac{\partial u}{\partial y}+\frac{\rho_f}{\rho_{nf}}\frac{\partial p}{\partial x}, \tag{15}$$

$$\frac{\nu_{nf}}{\nu_f}Pr\nabla^2 v = u\frac{\partial v}{\partial x}+v\frac{\partial v}{\partial y}+\frac{\rho_f}{\rho_{nf}}\frac{\partial p}{\partial y}-\frac{(\rho\beta)_{nf}}{\rho_{nf}\beta_f}RaPrT+\frac{\rho_f}{\rho_{nf}}RaPr\left(R_bN_m+NrC\right), \tag{16}$$

$$\frac{\alpha_{nf}}{\alpha_f}\nabla^2 T = u\frac{\partial T}{\partial x}+v\frac{\partial T}{\partial y}, \tag{17}$$

$$\frac{1}{Le}\nabla^2 C = u\frac{\partial C}{\partial x}+v\frac{\partial C}{\partial y}+\frac{\sigma}{Le}N_m, \tag{18}$$

$$\frac{1}{Le}\nabla^2 N_m = \chi\left(u\frac{\partial N_m}{\partial x}+v\frac{\partial N_m}{\partial y}\right)+\frac{Pe}{Le}\left(N_m\nabla^2 C+\frac{\partial C}{\partial x}\frac{\partial N_m}{\partial x}+\frac{\partial C}{\partial y}\frac{\partial N_m}{\partial y}\right), \tag{19}$$

where $\chi=\frac{D_c}{D_n},\ \sigma=\frac{\delta n_0 L^2}{D_c\Delta C}$. N_m is the number of microorganisms. Prandtl, Rayleigh, bioconvection Rayleigh, Peclet numbers, buoyancy ratio parameter and Lewis numbers are given as [55]

$$Pr=\frac{\nu_f}{\alpha_f},\ Ra=\frac{g\beta_f\Delta TL^3}{\nu_f\alpha_f},\ R_b=\frac{\gamma\Delta\rho n_0}{\rho_f\beta_f\Delta T},\ Pe=\frac{bW_c}{D_n}, Nr=\frac{(\rho_s-\rho_f)\beta_s\Delta C}{\rho_f\beta_f\Delta T},\ Le=\frac{\alpha_f}{D_c}. \tag{20}$$

Stream function $(u,v)=\left(\frac{\partial\psi}{\partial y},-\frac{\partial\psi}{\partial x}\right)$ and the vorticity $\omega=\frac{\partial v}{\partial x}-\frac{\partial u}{\partial y}$ are used to eliminate the pressure terms in the momentum equations and the governing equations of this problem are acquired by

$$\nabla^2\psi=-\omega, \tag{21}$$

$$\frac{\alpha_{nf}}{\alpha_f}\nabla^2 T = u\frac{\partial T}{\partial x}+v\frac{\partial T}{\partial y}, \tag{22}$$

$$\frac{1}{Le}\nabla^2 C = u\frac{\partial C}{\partial x}+v\frac{\partial C}{\partial y}+\frac{\sigma}{Le}N_m, \tag{23}$$

$$\frac{1}{Le}\nabla^2 N_m = \chi\left(u\frac{\partial N_m}{\partial x}+v\frac{\partial N_m}{\partial y}\right)+\frac{Pe}{Le}\left(N_m\nabla^2 C+\frac{\partial C}{\partial x}\frac{\partial N_m}{\partial x}+\frac{\partial C}{\partial y}\frac{\partial N_m}{\partial y}\right), \tag{24}$$

$$\frac{\nu_{nf}}{\nu_f}Pr\nabla^2\omega = u\frac{\partial\omega}{\partial x}+v\frac{\partial\omega}{\partial y}-\frac{(\rho\beta)_{nf}}{\rho_{nf}\beta_f}RaPr\frac{\partial T}{\partial x}+\frac{\rho_f}{\rho_{nf}}RaPr\left(R_b\frac{\partial N_m}{\partial x}+Nr\frac{\partial C}{\partial x}\right) \tag{25}$$

with non-dimensional boundary conditions given as [34,56]

on the left wall :
$u = v = \psi = 0, T = 1, C = N_m = 1,$
on the right wall :
$u = v = \psi = 0 = T, C = N_m = 1,$
on the bottom wall :
$u = v = \psi = 0, \frac{\partial T}{\partial y} = 0, C = 1, PeN_m \frac{\partial C}{\partial y} = \frac{\partial N_m}{\partial y},$
on the top wall :
$u = v = \psi = 0, \frac{\partial T}{\partial y} = \frac{\partial C}{\partial y} = \frac{\partial N_m}{\partial y} = 0.$

The average Nusselt and the Sherwood numbers, and the average density of bacteria along the heated wall are evaluated by [34]

$$\overline{Nu} = -\frac{k_{nf}}{k_f}\int_0^1 \frac{\partial T}{\partial x}dy, \quad \overline{Sh} = -\int_0^1 \frac{\partial C}{\partial x}dy, \ \overline{N_m} = -\int_0^1 \frac{\partial N_m}{\partial x}dy. \tag{26}$$

3. Numerical Method

The radial basis function (RBF) method is a powerful numerical technique for finding solutions to partial differential equations. In addition to its efficiency, it is easy to implement both regular and irregular geometries [57]. Furthermore, it is more practical to obtain differentiation matrices with the RBF method compared to FDM and FEM. The most important advantage of the RBF method is its meshless nature. Unlike traditional methods like FEM or FVM, RBF does not need a structured grid or a complex mesh. By removing the need for mesh generation, we avoid mesh-related errors and difficulties. This approach provides high accuracy and saves computational time, especially when calculating the fluid flow and bacteria movement near the sinusoidal walls.

RBF method [58,59] is implemented to approximate the unknown ξ with the use of RBF *g(r)* given as

$$\xi(x,y) = \sum_{i=1}^{N_d+N_b} \tilde{a}_i g(\| (x,y) - (x_i, y_i) \|). \tag{27}$$

Here, N_d and N_b are the discretized domain and boundary points, respectively. $r = \left\|(x,y) - (x_i, y_i)\right\|_2$ represents the Euclidean norm of the field (x,y) and discretized points (x_i, y_i). The discretized form of Eq. (27) is $\xi = G\tilde{a}$, in which the dimensions of matrix G and the vector $\tilde{a}$ are $(N_d + N_b)\times(N_d + N_b)$ and $(N_d + N_b)\times 1$, respectively.

The partial derivatives of ξ acquired from the equations Eq. (27) and the discretized form can be expressed as follows:

$$\xi_{x,y} = G_{x,y}G^{-1}\xi, \quad \xi_{xx,yy} = G_{xx,yy}G^{-1}\xi, \tag{28}$$

wherein the matrices G_x, G_y, $G_{\{xx,yy\}}$ are obtained by taking the corresponding partial derivatives of *g(r)*.

In the current study, polyharmonic spline RBF $g(r) = r^7$ is employed to solve the system of Eqs. (21)-(25) and the discretized form can be stated as

$$P_L\psi^{k+1} = -\omega^k, \tag{29}$$

$$\left(\frac{\alpha_{nf}}{\alpha_f}P_L - K\right)T^{k+1} = 0, \tag{30}$$

$$\left(P_L - LeK\right)C^{k+1} = \sigma N_m^k, \tag{31}$$

$$\left(P_L - Le\chi K - PeP_L[C^{k+1}]_d\right)N_m^{k+1} - Pe(P_x[C^{k+1}]_d P_x + [P_yC^{k+1}]_d P_y)N_m^{k+1} = 0, \tag{32}$$

$$\left(\frac{\nu_{nf}}{\nu_f}PrP_L - K\right)\omega^{k+1} = -\frac{(\rho\beta)_{nf}}{\rho_{nf}\beta_f}RaPrP_xT^{k+1} + \frac{\rho_f}{\rho_{nf}}RaPr(R_bP_xN_m^{k+1} + NrP_xC^{k+1}), \tag{33}$$

where $K = ([P_y\psi]_d P_x + [P_x\psi]_d P_y)$, $P_x = G_xG^{-1}$, $P_y = G_yG^{-1}$ and $P_L = (G_{xx} + G_{yy})G^{-1}$. $[.]_d$ represents the diagonal matrix, k denotes the iteration level. The iterative solution procedure and the sequential steps of the numerical algorithm are illustrated in Figure 3. $\overline{Nu}, \overline{Sh}$ and $\overline{N_m}$ are computed utilizing the Composite Simpson's 1/3 rule for the integration.

4. Surface Fitting

Surface fitting is a mathematical process to model the relationship between a set of points in three-dimensional space (x, y, z). In this process, the datasets are utilized to find a smooth surface that best fits these data. The surface is formulated by $z = f_{sf}(x, y)$ where f_{sf} is the fitting function. In this study, the cubic polynomial function

$$f_{sf}(x,y) = a_0 + a_1x + a_2y + a_3xy + a_4x^2 + a_5y^2 + a_6x^2y^2 + a_7x^2y + a_8xy^2 + a_9x^3 + a_{10}y^3 \tag{34}$$

is taken. In order to check the goodness of fit, the mean squared error (mse) is evaluated by

$$mse = \frac{\sum_{i=1}^{S_d} (z_i - f_{sf}(x_i, y_i))^2}{S_d} \tag{35}$$

where S_d is the size of the data and z_i is actual data.

5. Results

5.1. Validation and Grid Independence

To validate the accuracy of the RBF method, results of $\overline{Nu}$ and $|\psi|_{\max}$ are compared with the findings of [60] solved the natural convection of Al_2O_3 -water in an enclosure by taking $Ra=10^5$ at $Ha=0$. Table 3 depicts that our results are in good agreement with the results in [60].

Grid independence is also checked, and the results given in Table 4 indicate that 41×41 uniform mesh points satisfy the grid independence.

5.2. Numerical Results

In this study, numerical results obtained by RBF method are presented in terms of $\overline{Nu}$, $\overline{Sh}$ and $\overline{N_m}$ for different parameters in the ranges of $10^2 \le Ra \le 10^5, 10 \le R_b \le 100, 0.1 \le Pe \le 10, 1 \le Le \le 10, 0.1 \le Nr \le 1, 0 \le a \le 0.1$ and n_{sh} with a fixed $Pr = 6.8, \sigma = 1$ in Figures 4-5. In all these figures, results obtained by n_{sh} =3.7 and 8.6 are close to each other due to the μ_{nf} computations in Eq. (7). Also, the variations of physical parameters are presented in terms of contour plots of ψ, T, C and N_m for fixed n_{sh} =5.7 in Figures 6-10.

Figure 4a shows the effect of Ra and n_{sh} on the average numbers ($\overline{Nu}$, $\overline{Sh}$ and $\overline{N_m}$) for $R_b = 10, Pe = Nr = 0.5, Le = 1, a = 0.1, \chi = 2$. The rise in Ra enhances the heat transfer regardless of the nanoparticle shapes due to the transition from a conduction-dominated regime to a convection-dominated regime. Physically, a higher Ra signifies a stronger buoyancy force relative to the viscous resistance. Conversely, the increase in n_{sh} reduces the heat transfer. It is noted that spherical particles show the highest enhancement with the average $\overline{Nu}$ increasing by 313.6% as Ra increases from 10^2 to 10^5. Regarding the mass transfer characteristics, a reverse relationship is observed between Ra and $\overline{Sh}$. A rise in Ra declines $\overline{Sh}$ approximately 31% for each nanoparticle shape which indicates that the effect of the buoyancy-driven flow dominates over the localized geometric influences of the various nanoparticle shapes in this parameter range. As the thermal buoyancy force increases to 10^4, $\overline{N_m}$ sharply decreases, but a slight increase in $\overline{N_m}$ is observed when Ra rises 10^5. In Fig. 4b, bioconvection effect generated by MB is analyzed for different n_{sh} keeping $Ra = 10^4, Pe = Nr = 0.5, Le = 1, a = 0.1, \chi = 2$. The augmentation of R_b diminishes $\overline{Nu}$, but rises $\overline{Sh}$ and $\overline{N_m}$ for all nanoparticle shapes. Physically, buoyancy force weakens the natural convection strength, thereby reducing the heat transfer rate. The heat transfer is the highest for spherical and the lowest for the platelet nanoparticle shapes at R_b =10 due to the viscosity-shape interaction. On the contrary, mass transfer and average density of bacteria reach their maximum for platelet-shaped particles and their minimum for spherical ones. As R_b reaches to 100, the influence of nanoparticle shape reduces on these averages, since spherical shapes diminish $\overline{Nu}$ by 39.93% and enhance $\overline{Sh}$ by 40.30%. In comparison, platelet-shaped particles result in a 29.89% decrease in $\overline{Nu}$ and a 31.13% increase in $\overline{Sh}$. Figure 4c depicts the influence of Pe, which is the ratio of the velocities because of the swimming cell and diffusion of MB, keeping $Ra = 10^4, R_b = 10, Le = 1, Nr = 0.5, a = 0.1, \chi = 2$. Both Pe and n_{sh} show the same effects on the temperature gradient as in the augmentation of R_b and n_{sh} comparing to Fig. 4b, where the bioconvective interaction slightly suppresses the thermal buoyancy. The influence of Pe on the mass transfer is more pronounced for different nanoparticle shapes. From Pe =0.1 to Pe =0.5, $\overline{Sh}$ decreases since initial swimming motions disrupt the concentration stability. However, it increases from Pe =0.5 to Pe =1 for all n_{sh} as higher swimming speeds begin to effectively pump microorganisms toward the hot wall. When $1 \le Pe \le 10$, cylinder and platelet shapes diminish the mass transfer, whereas the others enhance it which shows that the nanoparticle shapes gain an important effect on the mass transfer for $1 \le Pe \le 10$. The average number of bacteria rises with an increment in Pe due to the effect of maximum swimming velocity of MB. Also, the highest value of $\overline{N_m}$ attains for spherical nanoparticles with 14245 %. In Fig. 4d, the variation of Le is examined for $Ra = 10^4, R_b = 10, Pe = Nr = 0.5, a = 0.1, \chi = 2$. The augmentation of Le improves the convective heat transfer and $\overline{Nu}$ is the highest for spherical shapes. The rise in Lewis number means that the diffusivity of nanoparticle decreases. For that reason, the mass transfer lessens for any nanoparticle shape with an increment Le, as reduced particle mobility promotes a wider the concentration boundary layer and weakens the gradient at the hot wall. However, for a fixed Le the increment in n_{sh} improves the mass transfer. An augmentation of Le reduces the average number of bacteria for all n_{sh}. Compared to nanoparticle shape impacts, it is noted that platalet-shaped particles (n_{sh} =5.7) exhibit the highest changes in this comparison, with a 5.38% increase in $\overline{Nu}$, 19.37% decrease in $\overline{Sh}$, and 5.44% decrease in $\overline{N_m}$.

The influence of the buoyancy ratio parameter for the different nanoparticle shapes keeping $Ra = 10^4, R_b = 10, Pe = 0.5, Le = 1, a = 0.1, \chi = 2$ in Fig. 5a. Since *Nr* is the ratio of buoyancy forces due to the nanoparticle concentration and thermal circulation, the rise in *Nr* decelerates the heat transfer, whereas accelerates the mass transfer for any n_{sh}. For a fixed *Nr* spherical nanoparticle causes $\overline{Nu}$ to attain the highest value, while the lowest values of $\overline{Sh}$ and $\overline{N_m}$ are obtained for spherical particles. This shows that spherical particles results in higher heat transfer but lower mass transport compared to non-spherical shapes. Figure 5b illustrates an alteration of the amplitude of the curved wall for $Ra = 10^4, R_b = 10, Pe = Nr = 0.5, Le = 1, \chi = 2.$ The augmentation of a increases all average numbers for any nanoparticle shape because a larger amplitude increases the surface area of the wall and creates more space for fluid circulation, which forces the fluid to interact more intensely with the boundaries. This geometric enhancement is particularly evident for platelet-shaped nanoparticles, where $\overline{Nu}$ and $\overline{Sh}$ increase by 33.47% and 24.10%, respectively. On the other hand, as n_{sh} rises with a fixed a, the heat transfer diminishes but the mass transfer and the average number of bacteria enhance. Fig. 5c represents the impacts of χ and n_{sh} for $Ra = 10^4, R_b = 10, Pe = Nr = 0.5, Le = 1, a = 0.1$. The increase in χ, which is defined by the increment of diffusivity of nanoparticle concentration or decrease in the diffusivity of MB, improves the heat transfer but weakens the mass transfer. $\overline{Sh}$ and $\overline{N_m}$ rise as n_{sh} increases for a fixed χ.

Figure 6 depicts the impact of Ra for fixed $R_b = 10$, $Pe = Nr = 0.5$, $Le = 1$ and n_{sh} =5.7 . As Ra increases, the main vortex of the flow moves to the right cold wall with an increasing magnitude because of the thermal buoyancy force. Thermal boundary layers become more distinct and thinner at the cold and hot walls as the stronger flow carries heat more rapidly across the cavity. Isoconcentration lines transition into circular patterns, and solutal boundary layers develop at the left, right and the bottom walls with an increment in Ra. This indicates that the intensified flow pushes the nanoparticles toward the boundaries. Augmentation of Ra causes MB to move down forming a circular shape with increasing magnitude. This shift is a direct result of the dragging effect from the main flow vortex; as the fluid circulation strengthens, it dominates the swimming motion of the bacteria, forcing them to follow the primary convective path and accumulate in the lower regions of the cavity.

Bioconvection Rayleigh number effect is analyzed holding $Ra = 10^4, Pe = Nr = 0.5, Le = 1$ and n_{sh} =5.7 in Figure 7. The rise in R_b forms a secondary vortex and squeezes the main vortex to the cold wall. This happens because R_b represents the downward force caused by MB. When this downward force becomes stronger, it pushes against the main upward thermal flow, forming a secondary circulation cell. The formation of the secondary vortex destroys the convective heat transfer and causes $\overline{Nu}$ to diminish as seen in Figure 4b. Isoconcentartion lines show the symmetric behaviour, but it is observed in Figure 4b that the increment in R_b improves the mass transfer. As R_b increases, MB move up. This upward shift is caused by the secondary vortex lifting the bacteria in certain regions of the cavity, overcoming their natural tendency to settle.

Figure 8 presents the influence of Pe fixing $Ra = 10^4, R_b = 10, Nr = 0.5, Le = 1$ and n_{sh} =5.7. As Pe rises, the secondary vortex occurs at the left part of the cavity. Physically, Pe represents the ratio of the microorganisms' swimming speed to the fluid's thermal diffusion. A higher Pe means the bacteria are swimming faster, creating their own local current that pushes against the main thermal flow. Because of this new secondary vortex, isolines of *T, C* and N_m show similar behaviors to the R_b case. The interaction between the thermal buoyancy and the active swimming of the bacteria disrupts the heat flow, leading to a decrease in $\overline{Nu}$ shown in Figure 4c.

In Figure 9, the variation of Le is examined for $Ra = 10^4, R_b = 10, Pe = Nr = 0.5$ and n_{sh} =5.7. The augmentation of Le does not show the significant effect on the contours of ψ and T. This is because Le primarily affects the rate of mass diffusion rather than the thermal buoyancy that drives the fluid motion. Since flow has only one circulation, the isoconcentration lines move to center of the cavity forming a cell and the similar behavior is observed for MB.

The impact of buoyancy ratio parameter, which represents the relative strength of buoyancy caused by nanoparticle concentration compared to thermal buoyancy, is shown in Figure 10 keeping $Ra = 10^4, R_b = 10, Pe = 0.5, Le = 1$ and n_{sh} =5.7. An increase in *Nr* leads to the formation of the secondary vortex. Since the magnitude of the secondary vortex is small, the contours of *T, C* and N_m do not significantly affect with the augmentation of the buoyancy ratio. As a results, while the added buoyancy makes the fluid spin faster, it is not yet strong enough to reshape the overall distribution of heat and particles within the cavity.

5.3. Comparison with Similar Studies

Our numerical results are compared with previous studies investigating the shape effects of Fe_3O_4 nanoparticles. Similar to the findings of Sheikholeslami and Shehzad [23] and Sheikholeslami et al. [25], who explored nanofluid behavior in permeable and curved enclosures, our study confirms that the nanoparticle shape factor significantly modulates the thermal performance. They reported that platelet-shaped nanoparticles consistently provide the maximum heat transfer enhancement due to their superior effective thermal conductivity compared to spherical particles. While the aforementioned studies focused on porous media and magnetic sources, the present work extends these observations to bioconvection flows involving magnetotactic bacteria. A notable agreement is found that non-spherical shapes (platelets) outperform spherical ones as the wall amplitude increases. However, it is important to note that for a fixed set of physical parameters, the values of the average Nusselt number are higher for spherical nanoparticles compared to platelet-shaped ones.

5.4. Fitting Results

A distinctive feature of the current approach is the transition from numerical simulation to predictive algebraic modeling. By implementing the cubic surface fitting technique, the discrete numerical results are transformed into explicit mathematical functions. In order to find the fitting functions of $\overline{Nu}$, $\overline{Sh}$, $\overline{N_m}$ and ψ_{min} depending on each physical parameter (Ra, R_b, Pe, Le) and n_{sh}, four datasets are generated by implementing RBF method for fixed $Nr = 0.5, a = 0.1$ and $\chi = 2$. In each dataset (DS) n_{sh}, Nr, a and χ are taken as [3,3.7,4.9,5.7,8.6], 0.5, 0.1 and 2, respectively, but the ranges of the other parameters are set by

DS1:
$Ra = [10^2, 10^3, 10^4, 10^5], R_b = 10, Pe = 0.5, Le = 1$
DS2:
$R_b = [10, [25:25:100]], Ra = 10^4, Pe = 0.5, Le = 1$
DS3:
$Pe = [0.1, 0.5, 1, [2:2:10]], Ra = 10^4, R_b = 10, Le = 1$
DS4:
$Le = [0.1, 0.5, 1, 10], Ra = 10^4, R_b = 10, Pe = 0.5$

The obtained cubic fitting functions of $\overline{Nu}$ and $\overline{Sh}$ are found as

$$\begin{aligned} f_{\overline{Nu}}(Ra, n_{sh}) &= 0.008Ra - 0.0002n_{sh}Ra + 0.1146n_{sh}^2 - 0.0114n_{sh}^3, \\ f_{\overline{Sh}}(Ra, n_{sh}) &= 0.002Ra + 0.0381n_{sh}^2 - 0.0038n_{sh}^3, \end{aligned} \tag{36}$$

$$\begin{aligned} f_{\overline{Nu}}(R_b, n_{sh}) &= 4.2480 - 0.1091R_b - 0.2855n_{sh} + 0.0161R_b n_{sh} + 0.0013R_b^2 - 0.0203n_{sh}^2 - 0.0001n_{sh}R_b^2 - 0.0013n_{sh}^2 R_b + 0.0045n_{sh}^3, \\ f_{\overline{Sh}}(R_b, n_{sh}) &= 0.2452 + 0.0067R_b + 0.0142n_{sh} - 0.0007n_{sh}R_b - 0.0001R_b^2 + 0.0012n_{sh}^2 + 0.0001n_{sh}^2 R_b - 0.0002n_{sh}^3, \end{aligned} \tag{37}$$

$$\begin{aligned} f_{\overline{Nu}}(Pe, n_{sh}) &= 3.5811 - 1.1133Pe - 0.1202n_{sh} + 0.1642n_{sh}Pe + 0.1468Pe^2 - 0.0408n_{sh}^2 + 0.0009n_{sh}^2 Pe^2 - 0.0117n_{sh}Pe^2 - 0.0133n_{sh}^2 Pe \\ &\quad - 0.006Pe^3 + 0.0052n_{sh}^3, \\ f_{\overline{Sh}}(Pe, n_{sh}) &= 0.2917 + 0.0553Pe + 0.0157n_{sh} - 0.0084n_{sh}Pe - 0.0069Pe^2 + 0.0004n_{sh}Pe^2 + 0.0007n_{sh}^2 Pe + 0.0003Pe^3 - 0.0001n_{sh}^3, \end{aligned} \tag{38}$$

$$\begin{aligned} f_{\overline{Nu}}(Le, n_{sh}) &= 2.3062 + 0.5n_{sh} - 0.0035n_{sh}Le + 0.0096Le^2 - 0.1574 + 0.0002n_{sh}Le^2 + 0.0002n_{sh}^2 Le - 0.0008Le^3 + 0.012n_{sh}^3, \\ f_{\overline{Sh}}(Le, n_{sh}) &= 0.3303 + 0.0007n_{sh} - 0.0074n_{sh}Le + 0.0001Le^2 + 0.0036n_{sh}^2 + 0.0004n_{sh}Le^2 + 0.0006n_{sh}^2 Le - 0.0004n_{sh}^3. \end{aligned} \tag{39}$$

These obtained Eqs. (36)-(39) serve as a practical tool for researchers to estimate the average Nusselt and Sherwood numbers without the need for conducting computationally intensive simulations for every parameter combination.
Figures 11-14 depict the fitting surfaces of $\overline{Nu}$, $\overline{Sh}$, $\overline{N_m}$ and ψ_{min} for n_{sh} and the other parameters. In these figures, * and ∘ represent the numerical RBF results and fitting values, respectively. Mean squared error is provided for each figure to quantify the accuracy of the model. It is observed that the numerical results are fitted on the surfaces with a small mse, which indicates a best fit scenario. This high level of accuracy proves that the RBF model successfully captures the non-linear relationship between the particle shapes (from spheres to platelets) and the resulting transport efficiency. Consequently, these fitting surfaces can be used as reliable predictive tools for designing nanofluid systems without the need for further expensive simulations.

5.5. Case Study

This subsection provides a case study to demonstrate how these parameters can be connected for practical engineering applications such as in a targeted drug delivery system or a micro-bioreactor.

1. High-Efficiency Thermal Management: In applications such as electronic device cooling, maximizing the heat transfer rate is the primary objective. The optimal operation requires a high Rayleigh number ($Ra = 10^5$) and the use of spherical nanoparticles, which provides a 313.6% increase in thermal performance. In this scenario, the bioconvection Rayleigh number should be kept at lower levels ($R_b \le 10$) to prevent the formation of secondary vortices that suppress primary thermal circulation.
   While spherical particles provide the highest value of $\overline{Nu}$ under fixed conditions, platelet-shaped nanoparticles show the highest sensitivity to wall amplitude. Therefore, in a system with high geometric complexity (large a), platelets should be preferred to enhance the heat transfer rate.

2. Targeted Bio-Mass Transport: For biomedical applications involving magnetotactic bacteria, such as targeted drug delivery, maximizing the mass transfer rate and bacterial density is critical. The results indicate that platelet-shaped nanoparticles should be preferred over spherical ones, as they enhance the Sherwood number. The system should be maintained at a high bioconvection Rayleigh number $(R_b = 100)$, Peclet number $(Pe = 10)$ and the amplitude of the wall ($a=1$) which increases the average density of bacteria and the mass transfer rate.
3. The Integrated Roadmap: By utilizing the derived fitting functions, an operator can input the desired thermal load and required bacterial flux to determine the necessary wall amplitude and nanoparticle shape factor.

4. Conclusions

In this study, the bioconvection flow of a magnetite–water nanofluid containing MB is numerically investigated within a curved enclosure. The primary focus is to evaluate how nanoparticle shapes, ranging from spherical to platelet, interact with physical parameters $Ra, R_b, Pe, Le, Nr, a,$ and χ. RBF method, supported by curve fitting, provides a robust framework for this analysis. The main findings of this research are given below:

- The impact of nanoparticle shape: Nanoparticle geometry is a primary determinant of transport efficiency. While spherical nanoparticles yield the highest heat transfer rates, platelet-shaped nanoparticles outperform others in mass transfer and bacterial density. Notably, for a fixed wall amplitude $(a = 0.1)$, platelet shapes demonstrate a 33.47% increase in $\overline{Nu}$ and a 24.10% increase in $\overline{Sh}$, highlighting their superior sensitivity to surface curvature.
- The impact of Rayleigh and Bioconvection numbers: The intensification of thermal buoyancy (Ra) significantly boosts heat transfer; for spherical particles, an increase in Ra leads to a 313.43% rise in $\overline{Nu}$. Conversely, increasing R_b from 10 to 50 creates a secondary vortex that opposes the primary flow. This interference reduces heat transfer but improves the average density of bacteria for all shapes, with platelets showing the most significant accumulation.
- The impact of Peclet number: Peclet number plays a dominant role in microorganism distribution, where the average bacterial density for spherical shapes is enhanced by 14245% as Pe increases. Platelet and cylinder-shaped nanoparticles diminish the mass transfer rate, but other shapes enhances it for $1 \le Pe \le 10$.
- The impact of Lewis number: Higher Le values lead to a decrease in $\overline{Sh}$ but increase in $\overline{Nu}$ for each particle.
- Curve fitting: The study confirms that the RBF method, combined with curve fitting, is a highly precise predictive tool. The numerical results are fitted to surfaces with a small mse, proving that the model can reliably forecast transport coefficients across the entire range of nanoparticle shapes and physical parameters.

The findings of this study offer significant insights into the design of bio-microfluidic devices. Specifically, the high heat transfer efficiency observed with spherical nanoparticles suggests their suitability for high-performance cooling systems, whereas platelet-shaped nanoparticles are more effective for mass transfer applications, such as targeted drug delivery systems utilizing magnetotactic bacteria. These results can guide engineers in selecting optimal nanoparticle shapes to control thermal and solutal gradients in curved-geometry micro-channels. Furthermore, the developed surface fitting models offer a computationally efficient alternative for predicting system behavior without the need for exhaustive numerical simulations. Future research could extend this model to unsteady flow conditions or examine the influence of variable magnetic field orientations to further enhance the control over bacterial movement and heat distribution. Additionally, integrating artificial neural network (ANN) models to predict complex interactions in hybrid nanofluids.

Funding

This research did not receive any specific grant from funding agencies in the public, commercial, or not-for-profit sectors.

Conflicts of interest

The authors declare that they have no known competing financial interests or personal relationships that could have appeared to influence the work reported in this paper.

References

1. Choi, S. U. S., “Enhancing thermal conductivity of fluids with nanoparticles”, *ASME International Mechanical Engineering Congress and Exposition*, American Society of Mechanical Engineers, pp. 99–105 (1995).
2. Gümgüm, S. and Tezer-Sezgin, M., “DRBEM solution of natural convection flow of nanofluids with a heat source”, *Engineering Analysis with Boundary Elements*, **34**(8), pp. 727–737 (2010). https://doi.org/10.1016/j.enganabound.2010.03.006.
3. Jalili, B., Ghafoori, H., and Jalili, P., “Investigation of carbon nano-tube (CNT) particles effect on the performance of a refrigeration cycle”, *International Journal of Material Science Innovations*, **2**(1), pp. 8–17 (2014).

4. Sheikholeslami, M. and Ellahi, R., "Three dimensional mesoscopic simulation of magnetic field effect on natural convection of nanofluid", *International Journal of Heat and Mass Transfer*, **89**, pp. 799–808 (2015). https://doi.org/10.1016/j.ijheatmasstransfer.2015.05.110.
5. Pekmen Geridonmez, B., "RBF simulation of natural convection in a nanofluid-filled cavity", *AIMS Mathematics*, **1**, pp. 195–207 (2016). https://doi.org/10.3934/Math.2016.3.195.
6. Sheikholeslami, M., "New computational approach for exergy and entropy analysis of nanofluid under the impact of Lorentz force through a porous media", *Computer Methods in Applied Mechanics and Engineering*, **344**, pp. 319–333 (2019). https://doi.org/10.1016/j.cma.2018.09.044.
7. Sheikholeslami, M., "Numerical approach for MHD Al2O3-water nanofluid transportation inside a permeable medium using innovative computer method", *Computer Methods in Applied Mechanics and Engineering*, **344**, pp. 306–318 (2019). https://doi.org/10.1016/j.cma.2018.09.042.
8. Sayyou, H., Belabid, J., Öztop, H. F., et al., "Effects of vibration on natural convection in a square inclined porous enclosure filled with Cu-water nanofluid", *International Journal of Numerical Methods for Heat & Fluid Flow*, **34**(6), pp. 2399–2428 (2024). https://doi.org/10.1108/HFF-01-2024-0074.
9. Jafaripournimchahi, A., Shateri, A., Jalili, B.,et al., "The effects of magnetic field and thermal radiation on the mixed convection of Al2O3-Cu/water hybrid nanofluid over a permeable vertical flat plate", *Modern Physics Letters B*, **38**(25), p. 2450242 (2024). https://doi.org/10.1142/S0217984924502427.
10. Li, C., Roshani, H., Jalili, M.,et al., "Influence of hybrid nanofluids on entropy dynamics and transient thermal behavior in a finned enclosure with cylindrical obstruction", *Case Studies in Thermal Engineering*, **72**, p. 106339 (2025). https://doi.org/10.1016/j.csite.2025.106339.
11. Hajizadeh, S., Jalili, P., Jalili, B.,et al., "A novel approach to investigate the effect of hybrid nanofluids in a non-Newtonian Maxwell model on thermal management for medical engineering applications", *Modern Physics Letters B*, **39**(28), p. 2550140 (2025). https://doi.org/10.1142/S0217984925501404.
12. Khalatbari, S., Jalili, P., Jalili, B., et al., "Investigating the improvement of heat transfer and flow characteristics of hybrid nanofluids: A comprehensive review", *Proceedings of the Institution of Mechanical Engineers, Part E: Journal of Process Mechanical Engineering*, p. 09544089251318785 (2025). https://doi.org/10.1177/09544089251318785.
13. Majidi Zar, P., Shateri, A., Jalili, P., et al., "Radiative effects on 2D unsteady MHD Al 2 O 3 -water nanofluid flow between squeezing plates: A comparative study using AGM and HPM in Python", *ZAMM - Journal of Applied Mathematics and Mechanics / Zeitschrift für Angewandte Mathematik und Mechanik*, **105**(2), p. e202400546 (2025). https://doi.org/10.1002/zamm.202400546.
14. Dave, P. N. and Chopda, L. V., "Application of iron oxide nanomaterials for the removal of heavy metals", *Journal of Nanotechnology*, **2014**(1), p. 398569 (2014). https://doi.org/10.1155/2014/398569.
15. Luong, D., Sau, S., Kesharwani, P., et al., "Polyvalent folate-dendrimer-coated iron oxide theranostic nanoparticles for simultaneous magnetic resonance imaging and precise cancer cell targeting", *Biomacromolecules*, **18**(4), pp. 1197–1209 (2017). https://doi.org/10.1021/ACS.BIOMAC.6B01885.
16. Sheikholeslami, M., "Magnetic source impact on nanofluid heat transfer using CVFEM", *Neural Computing and Applications*, **30**(4), pp. 1055–1064 (2018). https://doi.org/10.1007/s00521-016-2740-7.
17. Abedini, A., Armaghani, T., and Chamkha, A. J., "MHD free convection heat transfer of a water–Fe3O4 nanofluid in a baffled C-shaped enclosure", *Journal of Thermal Analysis and Calorimetry 2018 135:1*, **135**(1), pp. 685–695 (2018). https://doi.org/10.1007/S10973-018-7225-8.
18. Battira, M. M., Brahmi, C., and Bessaih, R., "MHD natural convection of Fe3O4-water nanofluid in a cubic cavity", *Journal of Nano- and Electronic Physics*, **15**(5) (2023). https://doi.org/10.21272/JNEP.15(5).05032.
19. Jalili, P., Afifi, M. D., Jalili, B., et al., "Numerical study and comparison of two-dimensional ferrofluid flow in semi-porous channel under magnetic field", *International Journal of Engineering*, **36**(11), pp. 2087–2101 (2023). https://doi.org/10.5829/IJE.2023.36.11B.13.
20. Acharya, N., "Magnetically driven MWCNT-Fe3O4-water hybrid nanofluidic transport through a micro-wavy channel: A novel MEMS design for drug delivery application", *Materials Today Communications*, **38**, p. 107844 (2024). https://doi.org/10.1016/J.MTCOMM.2023.107844.
21. Timofeeva, E. V., Routbort, J. L., and Singh, D., "Particle shape effects on thermophysical properties of alumina nanofluids", *Journal of Applied Physics*, **106**(1) (2009). https://doi.org/10.1063/1.3155999.
22. Selimefendigil, F., Öztop, H. F., and Abu-Hamdeh, N., "Mixed convection due to rotating cylinder in an internally heated and flexible walled cavity filled with SiO2–water nanofluids: Effect of nanoparticle shape", *International Communications in Heat and Mass Transfer*, **71**, pp. 9–19 (2016). https://doi.org/10.1016/J.ICHEATMASSTRANSFER.2015.12.007.
23. Sheikholeslami, M. and Shehzad, S. A., "CVFEM for influence of external magnetic source on Fe3O4-H2O nanofluid behavior in a permeable cavity considering shape effect", *International Journal of Heat and Mass Transfer*, **115**, pp. 180–191 (2017). https://doi.org/10.1016/J.IJHEATMASSTRANSFER.2017.07.045.
24. Sheikholeslami, M., "Magnetic field influence on CuO–H2O nanofluid convective flow in a permeable cavity considering various shapes for nanoparticles", *International Journal of Hydrogen Energy*, **42**(31), pp. 19611–19621 (2017). https://doi.org/10.1016/J.IJHYDENE.2017.06.121.
25. Sheikholeslami, M., Shamlooei, M., and Moradi, R., "Numerical simulation for heat transfer intensification of nanofluid in a porous curved enclosure considering shape effect of Fe3O4 nanoparticles", *Chemical Engineering and Processing - Process Intensification*, **124**, pp. 71–82 (2018). https://doi.org/10.1016/J.CEP.2017.12.005.

26. Rafique, K., Mahmood, Z., Alqahtani, H., et al., "Various nanoparticle shapes and quadratic velocity impacts on entropy generation and MHD flow over a stretching sheet with joule heating", *Alexandria Engineering Journal*, **71**, pp. 147–159 (2023). https://doi.org/10.1016/J.AEJ.2023.03.021.
27. Kim, H., Do, Y., Ramachandran, S., et al., "Computational analysis of magnetohydrodynamic ternary-hybrid nanofluid flow and heat transfer inside a porous cavity with shape effects", *Physics of Fluids*, **36**(8) (2024). https://doi.org/10.1063/5.0222802.
28. Li, Y., Kalbasi, R., Karimipour, A., et al., "Using of artificial neural networks (ANNs) to predict the rheological behavior of magnesium oxide-water nanofluid in a different volume fraction of nanoparticles, temperatures, and shear rates", *Mathematical Methods in the Applied Sciences* (2020). https://doi.org/10.1002/mma.6418.
29. He, W., Ruhani, B., Toghraie, D., et al., "Using of artificial neural networks (ANNs) to predict the thermal conductivity of zinc oxide–silver (50%–50%)/water hybrid Newtonian nanofluid", *International Communications in Heat and Mass Transfer*, **116**, p. 104645 (2020). https://doi.org/10.1016/j.icheatmasstransfer.2020.104645.
30. Fuxi, S., Hamedi, S., Hajian, M., et al., "Addition of MWCNT-Al2O3 nanopowders to water- ethylene glycol (EG) base fluid for enhancing the thermal characteristics: Design an optimum feed-forward neural network", *Case Studies in Thermal Engineering*, **27**, p. 101293 (2021). https://doi.org/10.1016/J.CSITE.2021.101293.
31. Rostami, S., Toghraie, D., Esfahani, M. A., et al., "Predict the thermal conductivity of SiO2/water–ethylene glycol (50:50) hybrid nanofluid using artificial neural network", *Journal of Thermal Analysis and Calorimetry 2020 143:2*, **143**(2), pp. 1119–1128 (2020). https://doi.org/10.1007/S10973-020-09426-Z.
32. Eshgarf, H., Ahmadi Nadooshan, A., Raisi, A., et al., "Experimental examination of the properties of Fe3O4/water nanofluid, and an estimation of a correlation using an artificial neural network", *Journal of Molecular Liquids*, **374**, p. 121150 (2023). https://doi.org/10.1016/J.MOLLIQ.2022.121150.
33. Chari, F. N., Ganji, D. D., Mahboobtosi, M., et al., "Heat transfer analysis of GO/water nanofluid flow under the influence of Joule heating and chemical reactions with MHD: analytical and numerical concept", *Multiscale and Multidisciplinary Modeling, Experiments and Design*, **8**(5), p. 264 (2025). https://doi.org/10.1007/s41939-025-00843-x.
34. Sheremet, M. A. and Pop, I., "Thermo-bioconvection in a square porous cavity filled by oxytactic microorganisms", *Transport in Porous Media 2014 103:2*, **103**(2), pp. 191–205 (2014). https://doi.org/10.1007/S11242-014-0297-4.
35. Hussain, S. and Geridonmez, B. P., "Mixed bioconvection flow of Ag-MgO/water in the presence of oxytactic bacteria and inclined periodic magnetic field", *International Communications in Heat and Mass Transfer*, **134**, p. 106015 (2022). https://doi.org/10.1016/J.ICHEATMASSTRANSFER.2022.106015.
36. Habibishandiz, M., Saghir, Z., and Zahmatkesh, I., "Thermo-bioconvection performance of nanofluid containing oxytactic microorganisms inside a square porous cavity under constant and periodic temperature boundary conditions", *International Journal of Thermofluids*, **17**, p. 100269 (2023). https://doi.org/10.1016/J.IJFT.2022.100269.
37. Gurbuz-Caldag, M. and Pekmen, B., "Modeling on natural convection flow of Cu-water nanofluid with oxytactic bacteria and viscous dissipation", *Journal of Nanofluids*, **14**(6), pp. 869–882 (2025). https://doi.org/10.1166/jon.2025.2278.
38. Shahzad, F., Sagheer, M., and Hussain, S., "Transport of MHD nanofluid in a stratified medium containing gyrotactic microorganisms due to a stretching sheet", *Scientia Iranica*, **28**(6), pp. 3786–3805 (2021). https://doi.org/10.24200/SCI.2021.56459.4734.
39. Mil-Martínez, R., Vargas, R. O., Escandón, J. P., et al., "Thermal effect on the bioconvection dynamics of gravitactic microorganisms in a rectangular cavity", *Fluids 2022, Vol. 7, Page 113*, **7**(3), p. 113 (2022). https://doi.org/10.3390/FLUIDS7030113.
40. Alloui, I., Ouzani, R., Nguyen-Quang, T., et al., "Effect of density maximum of water on the stability of gravitactic convective motions in biothermal convection", *Environmental Fluid Mechanics 2024 24:2*, **24**(2), pp. 227–245 (2024). https://doi.org/10.1007/S10652-024-09981-1.
41. Naveed, M., Imran, M., and Majeed, M., "Analysis of Newtonian and Joule heating in a bioconvective Williamson nanofluid flow with gyrotactic microorganisms incorporating modified forms of Fourier's and Fick's laws", *Scientia Iranica* (2025). https://doi.org/10.24200/sci.2025.66898.10314.
42. Shateri, A., Ganji, A. M., Jalili, P., et al., "Utilizing Python for numerical analysis of bioconvection in magnetized Casson-Maxwell nanofluid systems with gyrotactic microorganisms: An investigation of dominant factors", *Results in Engineering*, **25**, p. 103760 (2025). https://doi.org/10.1016/j.rineng.2024.103760.
43. Pekmen Geridonmez, B. and Oztop, H., "Magnetotactic bacteria and Fe3O4–water in a wavy walled cavity", *International Journal of Numerical Methods for Heat & Fluid Flow*, **34**(4), pp. 1609–1630 (2024). https://doi.org/10.1108/HFF-08-2023-0465.
44. Ali, I., Peng, C., Khan, Z. M., et al., "An overview of heavy metal removal from wastewater using magnetotactic bacteria", *Journal of Chemical Technology & Biotechnology*, **93**(10), pp. 2817–2832 (2018). https://doi.org/10.1002/jctb.5648.
45. Pekmen, B. and Gurbuz-Caldag, M., "Numerical investigation on bioconvection flow in the presence of two concentrations", *Journal of Thermal Analysis and Calorimetry*, pp. 1–13 (2025). https://doi.org/10.1007/s10973-025-15015-9.
46. Chandra, P. and Das, R., "Finite-element-based machine-learning algorithm for studying gyrotactic-nanofluid flow via stretching surface", *International Journal for Numerical Methods in Fluids*, **95**(12), pp. 1888–1912 (2023). https://doi.org/10.1002/fld.5229.
47. Hussain, S., Öztop, H. F., Alsharif, A. M., et al., "Mixed bioconvection of nanofluid of oxytactic bacteria through a porous cavity with inlet and outlet under periodic magnetic field using artificial intelligence based on LightGBM

algorithm", *Thermal Science and Engineering Progress*, **50**, p. 102589 (2024). https://doi.org/10.1016/j.tsep.2024.102589.
48. Mahboobtosi, M., Ehsani, H., Ganji, A. M., et al., "AI-driven modeling of bioconvective nanofluid flow: An ANN approach to anisotropic slip and heat transfer in 3D systems", *International Communications in Heat and Mass Transfer*, **165**, p. 109035 (2025). https://doi.org/10.1016/j.icheatmasstransfer.2025.109035.
49. Kiratli, E., Gurbuz-Caldag, M., and Pekmen, B., "Neural network modeling on bioconvection flow subjected to the magnetic source", *2025 11th International Conference on Control, Decision and Information Technologies (CoDIT)*, IEEE, pp. 2645–2649 (2025) https://doi.org/10.1109/CoDIT66093.2025.11321376.
50. Khanafer, K., Vafai, K., and Lightstone, M., "Buoyancy-driven heat transfer enhancement in a two-dimensional enclosure utilizing nanofluids", *International Journal of Heat and Mass Transfer*, **46**(19), pp. 3639–3653 (2003). https://doi.org/10.1016/S0017-9310(03)00156-X.
51. Hamilton, R. L. and Crosser, O. K., "Thermal conductivity of heterogeneous two-component systems", *Industrial & Engineering Chemistry Fundamentals*, **1**(3), pp. 187–191 (1962). https://doi.org/10.1021/i160003a005.
52. Brinkman, H. C., "The viscosity of concentrated suspensions and solutions", *The Journal of Chemical Physics*, **20**(4), pp. 571–571 (1952). https://doi.org/10.1063/1.1700493.
53. Kuznetsov, A. V., "Thermo-bioconvection in a suspension of oxytactic bacteria", *International Communications in Heat and Mass Transfer*, **32**(8), pp. 991–999 (2005). https://doi.org/10.1016/J.ICHEATMASSTRANSFER.2004.11.005.
54. Reddy, N. and Murugesan, K., "Magnetic field influence on double-diffusive natural convection in a square cavity – A numerical study", *Numerical Heat Transfer, Part A: Applications*, **71**(4), pp. 448–475 (2017). https://doi.org/10.1080/10407782.2016.1277922.
55. Gurbuz-Caldag, M. and Pekmen, B., "Numerical investigation on Fe3O4-water nanofluid in the presence of magnetotactic bacteria", *Journal of Applied and Computational Mechanics*, **11**(2), pp. 467–484 (2025). https://doi.org/10.22055/jacm.2024.47204.4674.
56. Teamah, M. A., "Numerical simulation of double diffusive natural convection in rectangular enclosure in the presences of magnetic field and heat source", *International Journal of Thermal Sciences*, **47**(3), pp. 237–248 (2008). https://doi.org/10.1016/j.ijthermalsci.2007.02.003.
57. Kansa, E. J., Aldredge, R. C., and Ling, L., "Numerical simulation of two-dimensional combustion using mesh-free methods", *Engineering Analysis with Boundary Elements*, **33**(7), pp. 940–950 (2009). https://doi.org/10.1016/j.enganabound.2009.02.008.
58. Fasshauer, G. E., *Meshfree Approximation Methods with Matlab* (2007).
59. Fasshauer, G., Mccourt, M., and Scientific, W., *Kernel-Based Approximation Methods Using Matlab* (2015).
60. Ghasemi, B., Aminossadati, S., and Raisi, A., "Magnetic field effect on natural convection in a nanofluid-filled square enclosure", *International Journal of Thermal Sciences*, **50**(9), pp. 1748–1756 (2011). https://doi.org/10.1016/j.ijthermalsci.2011.04.010.

Figure and Table Captions

Figure 1. A graphical abstract

Figure 2. Problem configuration with boundary conditions.

Figure 3. Iteration Process.

Figure 4. Impacts of Ra (a.), R_b (b.), Pe (c.), Le (d.) and n_{sh} on $\overline{Nu}, \overline{Sh}, \overline{N_m}$.

Figure 5. Impacts of Nr (a.), a (b.), χ (c.) and n_{sh} on $\overline{Nu}, \overline{Sh}, \overline{N_m}$.

Figure 6. The effect of Ra for $R_b = 10, Pe = Nr = 0.5, Le = 1, n_{sh} = 5.7$.

Figure 7. The effect of R_b for $Ra = 10^4, Pe = Nr = 0.5, Le = 1, n_{sh} = 5.7$.

Figure 8. The effect of Pe for $Ra = 10^4, R_b = 10, Nr = 0.5, Le = 1, n_{sh} = 5.7$.

Figure 9. The effect of Le for $Ra = 10^4, R_b = 10, Pe = Nr = 0.5, n_{sh} = 5.7$.

Figure 10. The effect of Nr for $Ra = 10^4, R_b = 10, Pe = 0.5, Le = 1, n_{sh} = 5.7$.

Figure 11. Surface fitting of $\overline{Nu}, \overline{Sh}, \overline{N_m}, \psi_{min}$ for n_{sh} and Ra.

Figure 12. Surface fitting of $\overline{Nu}, \overline{Sh}, \overline{N_m}, \psi_{min}$ for n_{sh} and R_b.

Figure 13. Surface fitting of $\overline{Nu}, \overline{Sh}, \overline{N_m}, \psi_{min}$ for n_{sh} and Pe.

Figure 14. Surface fitting of $\overline{Nu}, \overline{Sh}, \overline{N_m}, \psi_{min}$ for n_{sh} and Le.

Table 1. Coefficients C_1 and C_2 corresponding to the different shape of nanoparticles [21].

Table 2. Thermophysical properties of water and Fe_3O_4 [43].

Table 3. Validation with Ghasemi et al. [60].

Table 4. Grid Independence for $Ra = 10^4, R_b = 10, Le = Pe = Nr = 1, a = 0.1, n_{sh} = 3.7$.

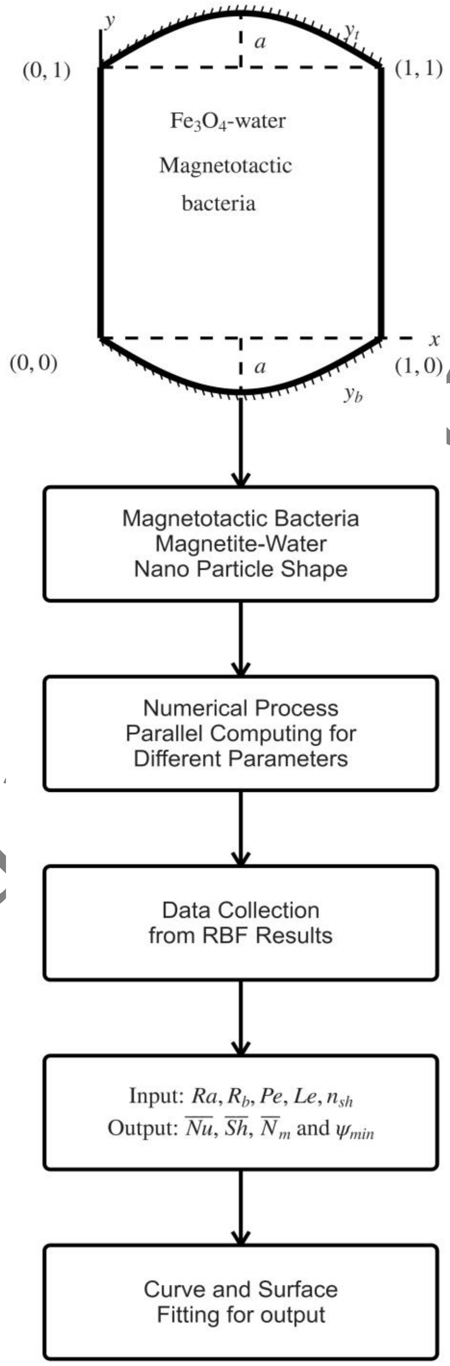

Figure 1. A graphical abstract

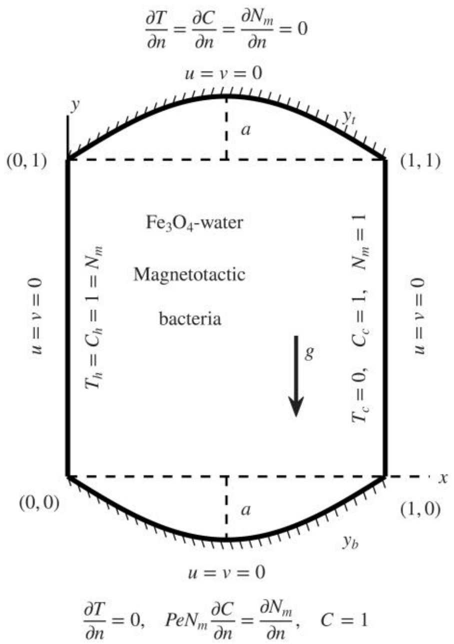

Figure 2. Problem configuration with boundary conditions.

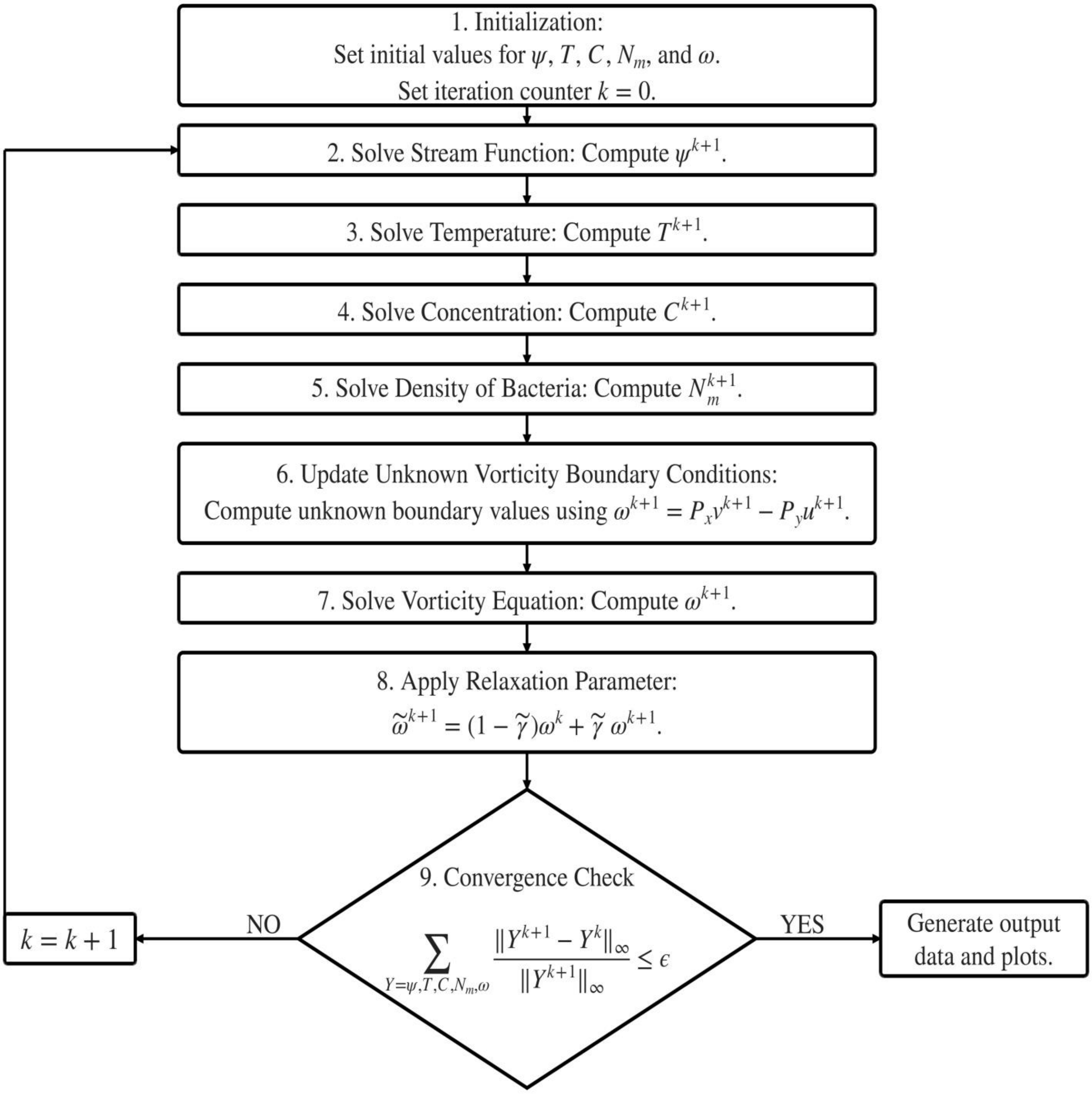

Figure 3. Iteration Process.

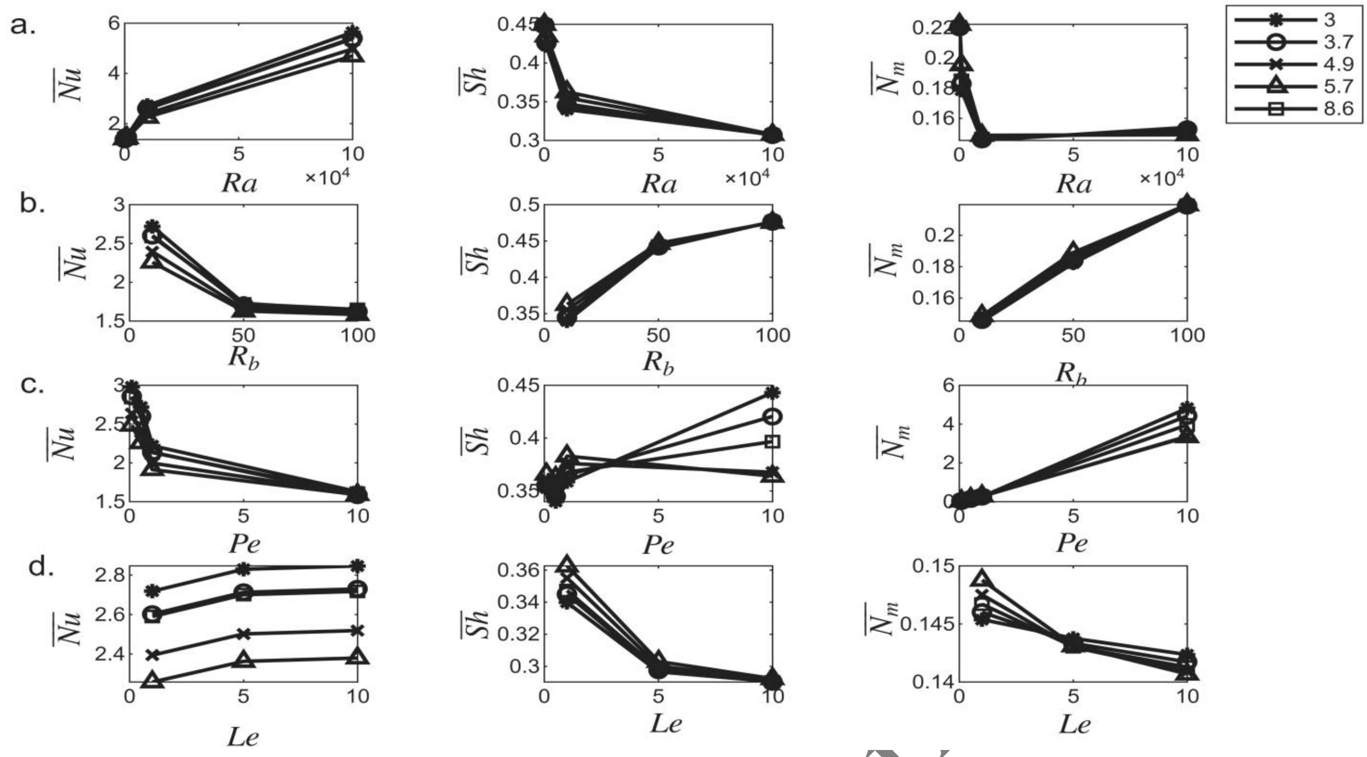

Figure 4. Impacts of *Ra* (a.), R_b (b.), *Pe* (c.), *Le* (d.) and n_{sh} on $\overline{Nu}$, $\overline{Sh}$, $\overline{N_m}$.

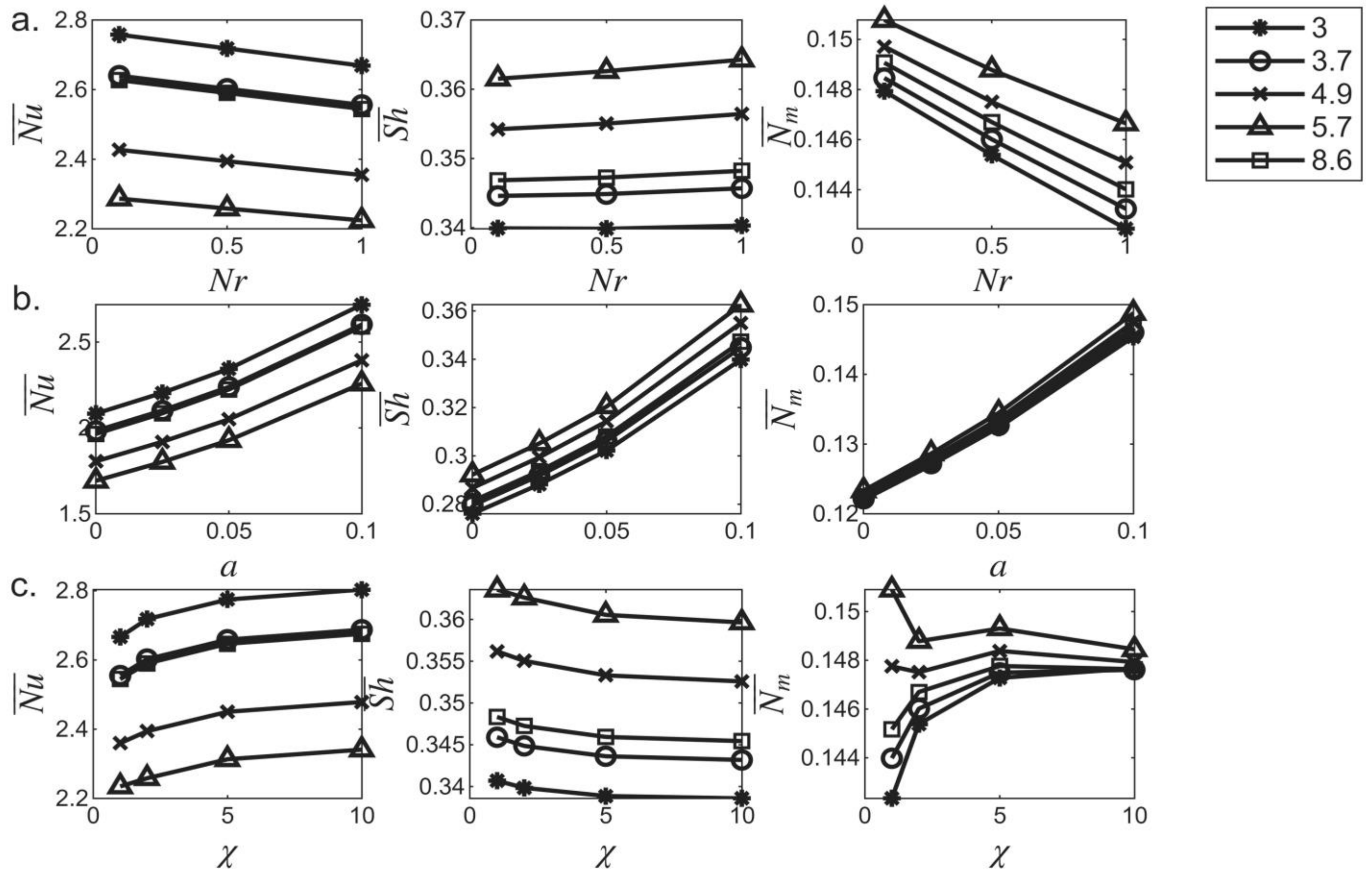

Figure 5. Impacts of *Nr* (a.), a (b.), χ (c.) and n_{sh} on $\overline{Nu}$, $\overline{Sh}$, $\overline{N_m}$.

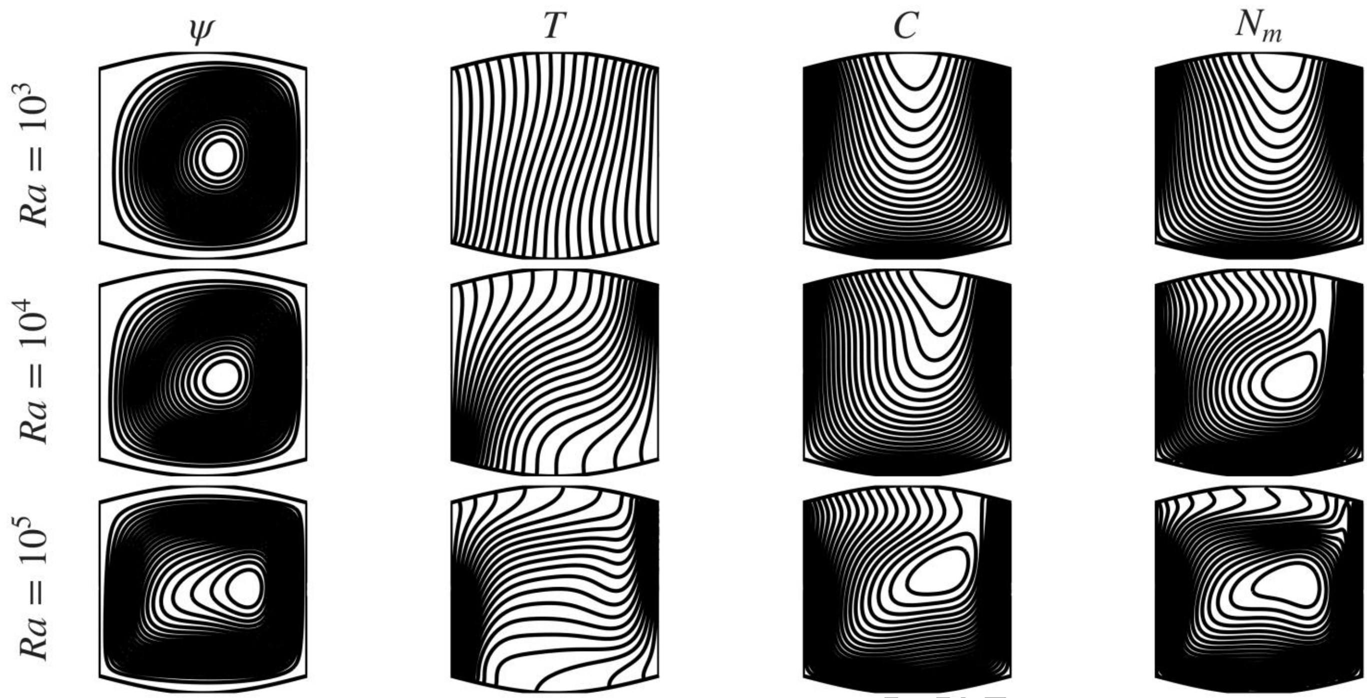

Figure 6. The effect of Ra for $R_b = 10, Pe = Nr = 0.5, Le = 1, n_{sh} = 5.7$.

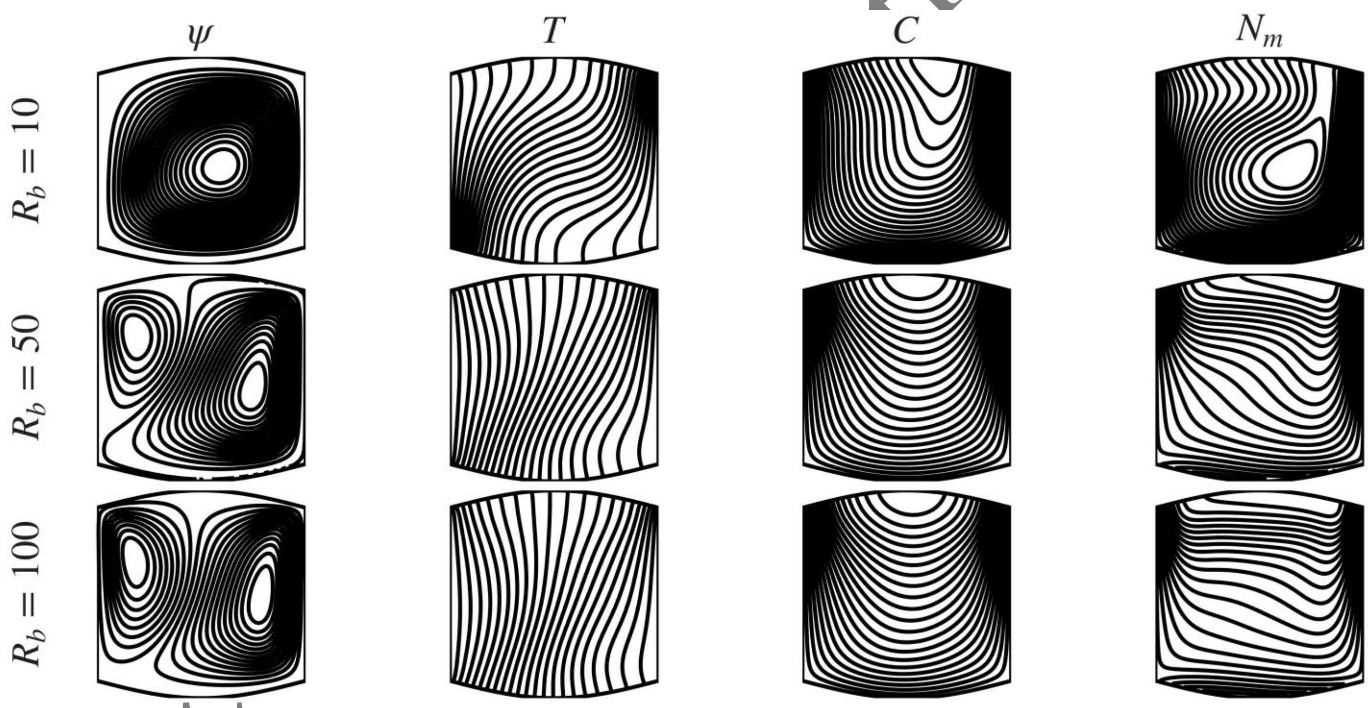

Figure 7. The effect of R_b for $Ra = 10^4, Pe = Nr = 0.5, Le = 1, n_{sh} = 5.7$.

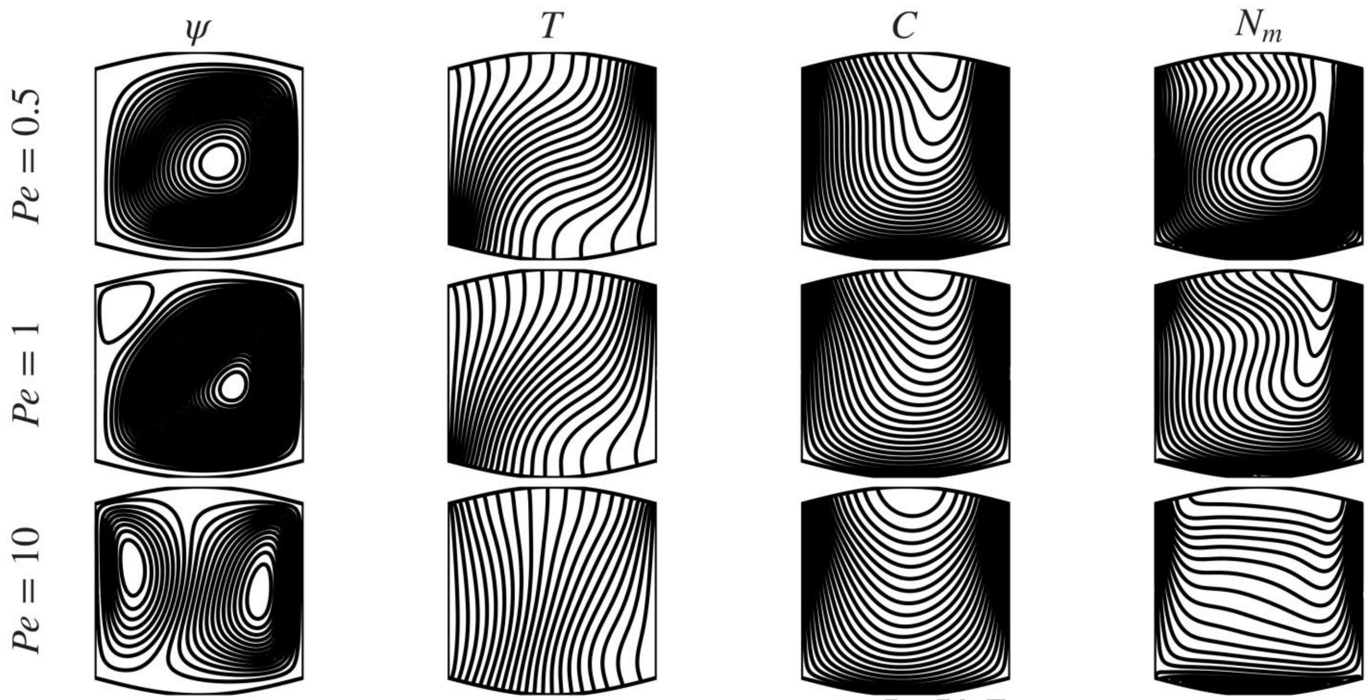

Figure 8. The effect of Pe for $Ra = 10^4, R_b = 10, Nr = 0.5, Le = 1, n_{sh} = 5.7$.

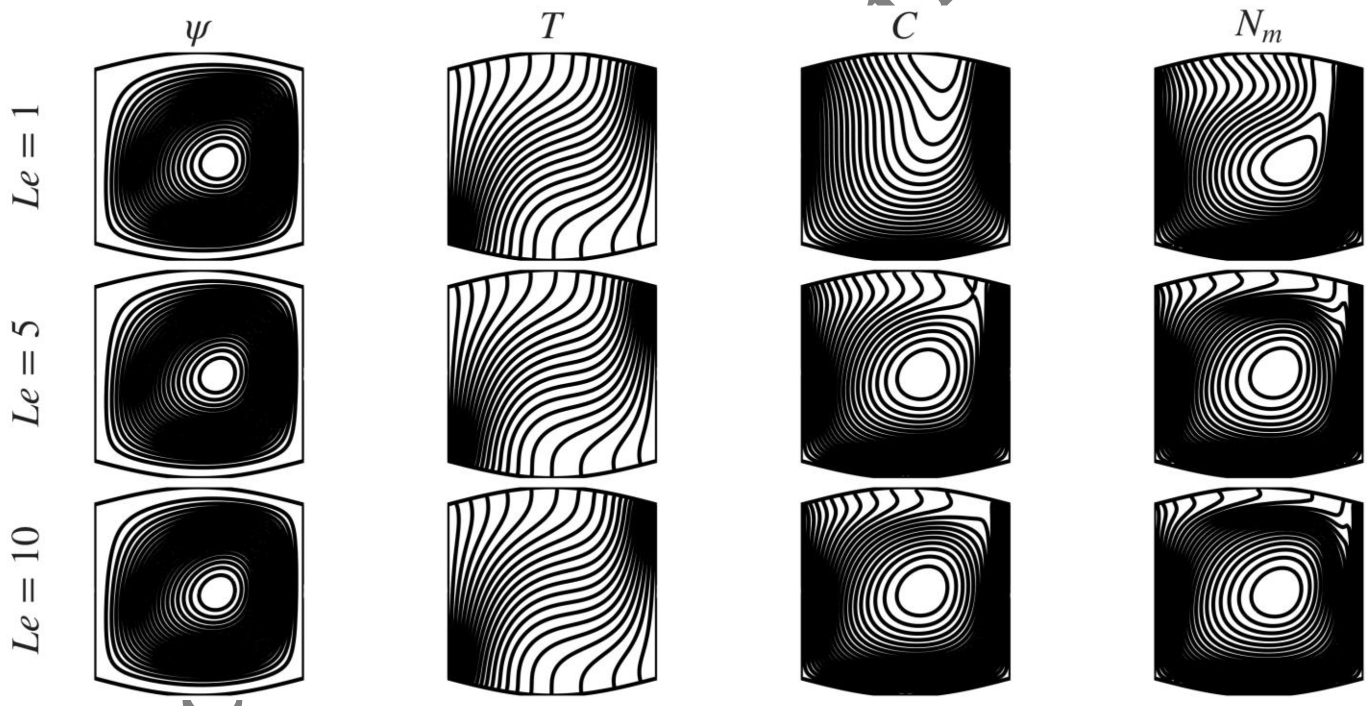

Figure 9. The effect of Le for $Ra = 10^4, R_b = 10, Pe = Nr = 0.5, n_{sh} = 5.7$.

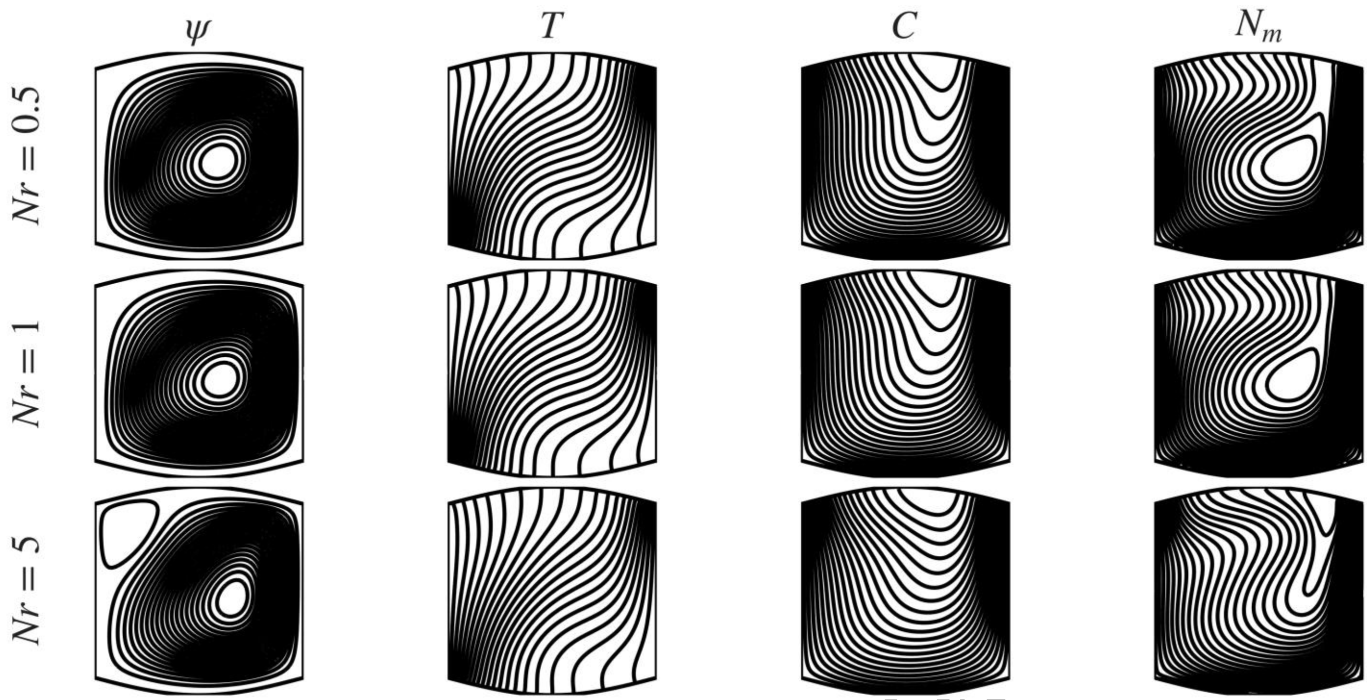

Figure 10. The effect of Nr for $Ra = 10^4, R_b = 10, Pe = 0.5, Le = 1, n_{sh} = 5.7$.

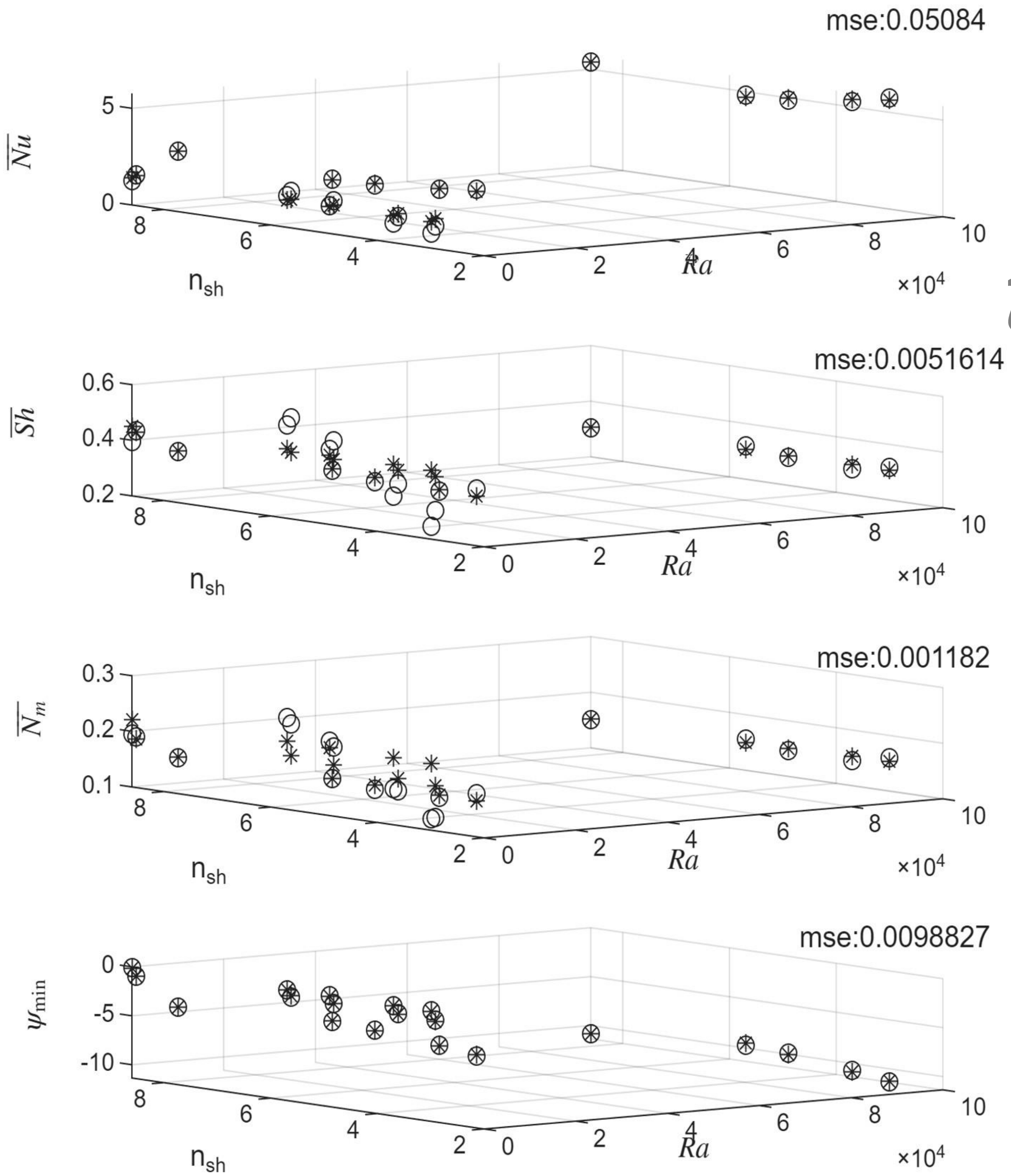

Figure 11. Surface fitting of $\overline{Nu}$, $\overline{Sh}$, $\overline{N_m}$, ψ_{min} for n_{sh} and Ra.

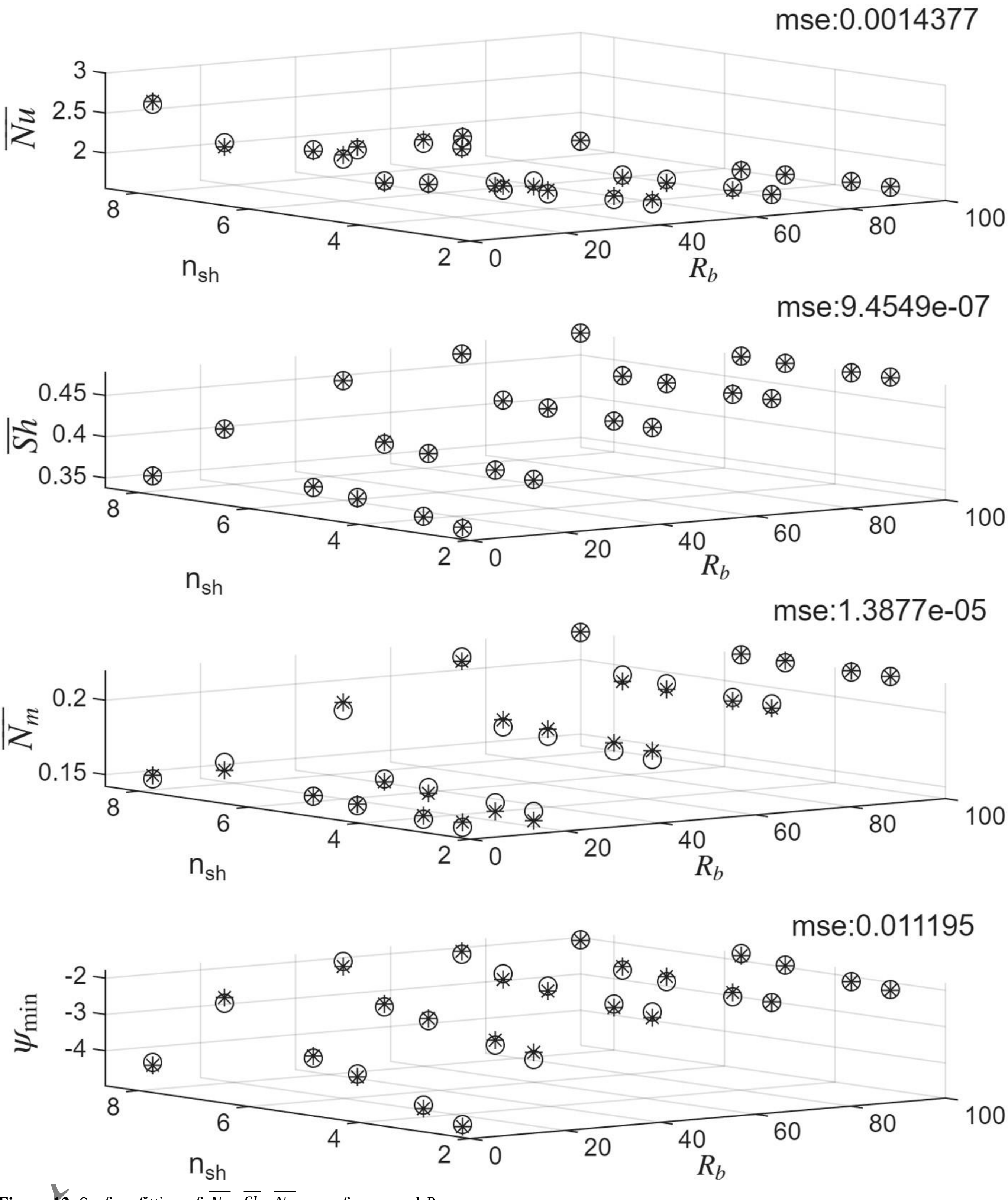

Figure 12. Surface fitting of $\overline{Nu}$, $\overline{Sh}$, $\overline{N_m}$, ψ_{min} for n_{sh} and R_b.

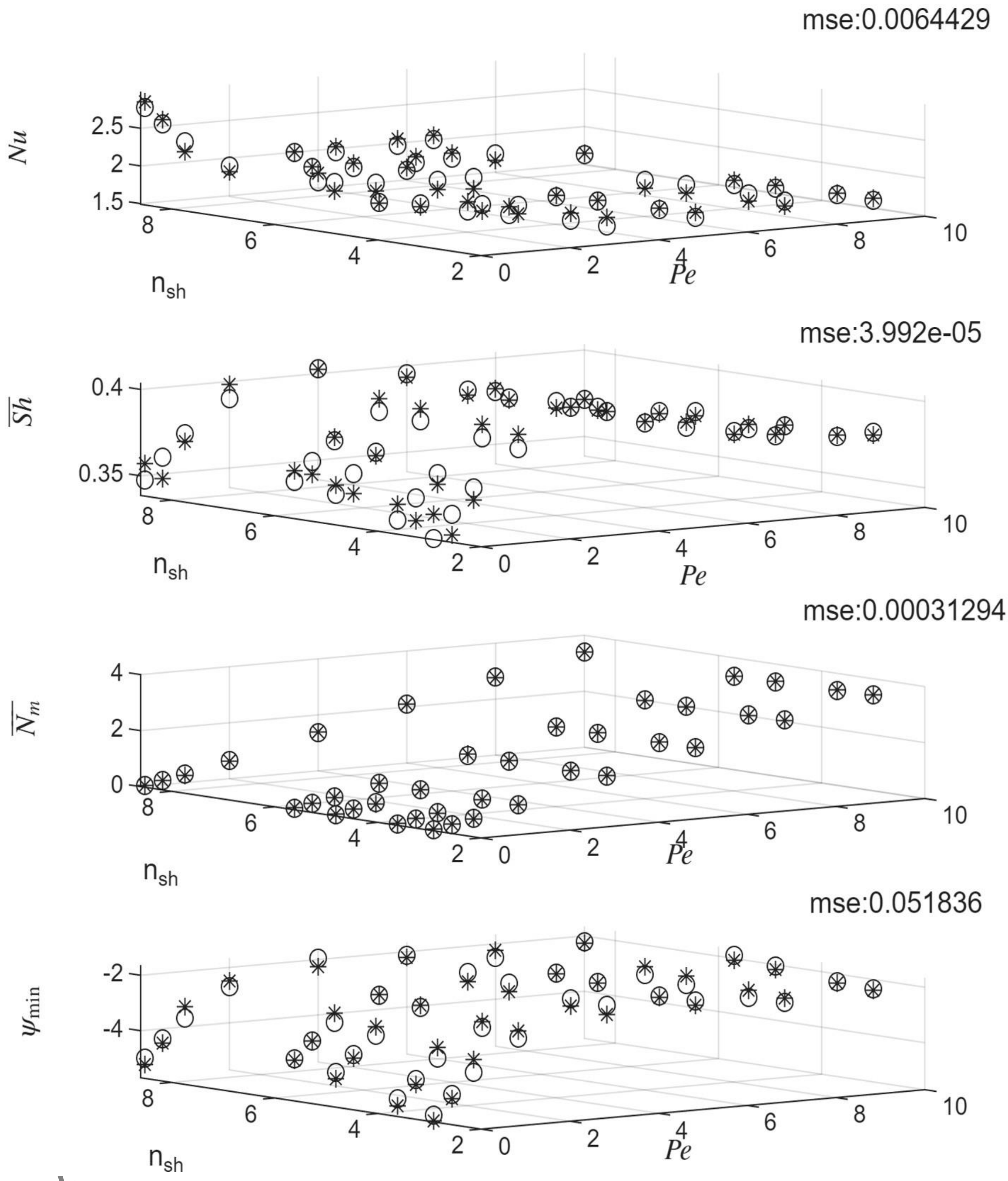

Figure 13. Surface fitting of $\overline{Nu}$, $\overline{Sh}$, $\overline{N_m}$, ψ_{min} for n_{sh} and Pe.

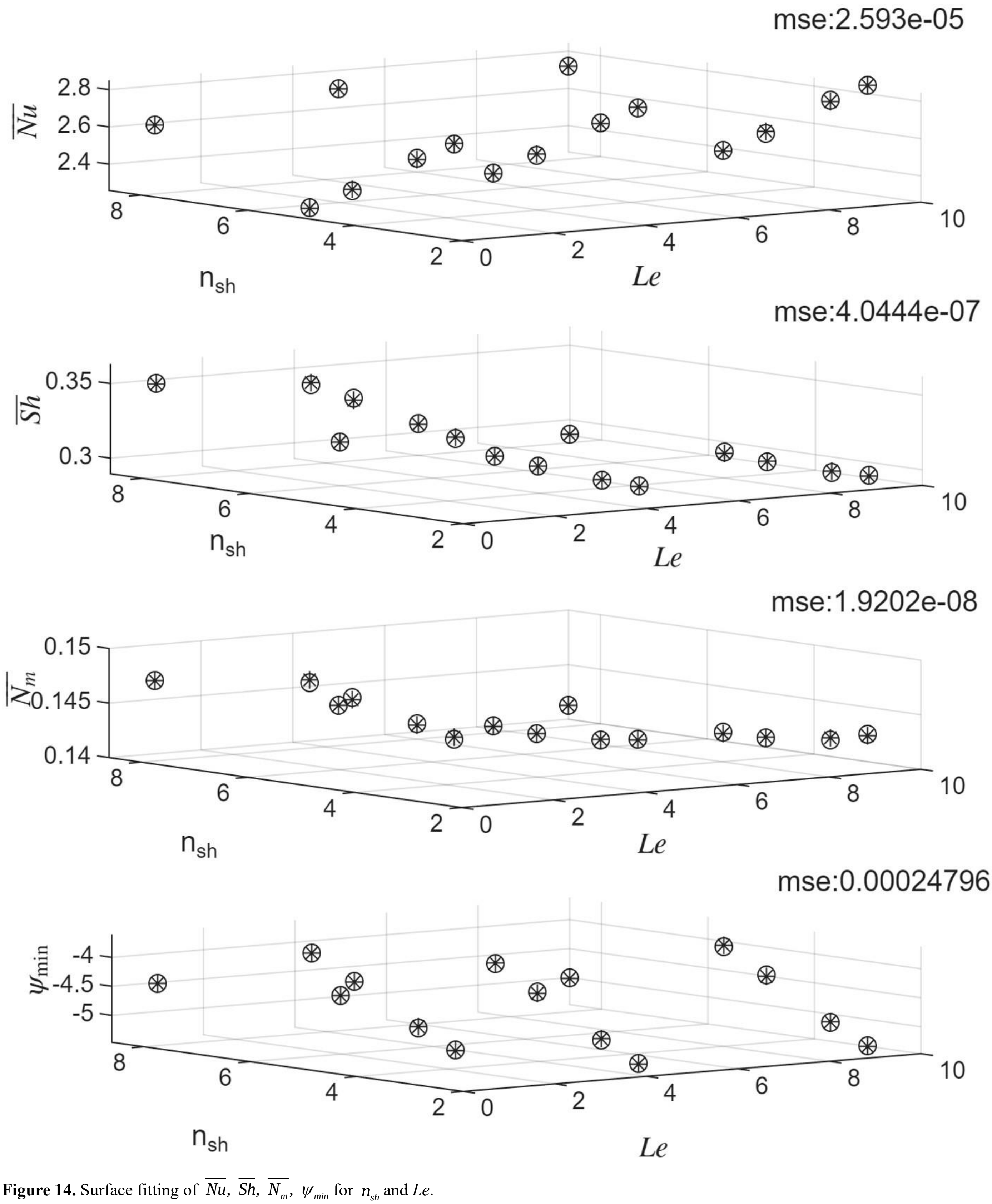

Figure 14. Surface fitting of $\overline{Nu}$, $\overline{Sh}$, $\overline{N_m}$, ψ_{min} for n_{sh} and Le.

Table 1. Coefficients C_1 and C_2 corresponding to the different shape of nanoparticles [21].

	Brick	Cylinder	Platelet	Blade
n_{sh}	3.7	4.9	5.7	8.6
C_1	1.9	13.15	37.1	14.6
C_2	471.4	904.4	612.6	123.3

Table 2. Thermophysical properties of water and Fe_3O_4 [43].

Property	Water	Fe_3O_4
$\rho\ (kg/m^3)$	997.1	5200
$c_p\ [J/(kgK)]$	4179	670
$k\ [W/(mK)]$	0.613	6
$\beta \times 10^{-5}\ (1/K)$	21	1.3

Table 3. Validation with Ghasemi et al. [60].

	Ghasemi et al. [60]		Current Study	
ϕ	$\lvert\psi\rvert_{\max}$	$\overline{Nu}$	$\lvert\psi\rvert_{\max}$	$\overline{Nu}$
0.02	11.313	4.820	11.309	4.752
0.04	11.561	4.896	11.560	4.834

Table 4. Grid Independence for $Ra = 10^4, R_b = 10, Le = Pe = Nr = 1, a = 0.1, n_{sh} = 3.7$.

$N \times N$	ψ_{min}	$\overline{Nu}$	$\overline{Sh}$
31×31	-3.574	2.279	0.381
41×41	-3.601	2.182	0.367
51×51	-3.613	2.121	0.359

Biographies

Merve Gurbuz-Caldag received her B.Sc. (2012) and Ph.D. (2017) degrees in Mathematics from the Middle East Technical University, Turkey. She is currently an Assistant Professor in the Department of Mathematics at TED University. Her research focuses on applied mathematics, numerical analysis, and computational fluid dynamics, with particular emphasis on magnetohydrodynamic (MHD) flows, Stokes flows, bioconvection phenomena, and heat–mass transfer problems.